OPEN ACCESS



Blanco DECam Bulge Survey (BDBS). VI. Extinction Maps Toward Southern Galactic Bulge Globular Clusters

Justin A. Kader 10, Catherine A. Pilachowski 10, Christian I. Johnson 20, R. Michael Rich 30, Michael D. Young 40,
Iulia T. Simion 50, William I. Clarkson 60, Scott Michael 10, Andrea Kunder 70, Anna Katherina Vivas 80,
Andreas J. Koch-Hansen 90, and Tommaso Marchetti 100

Department of Physics and Astronomy, 4129 Frederick Reines Hall, University of California, Irvine, CA 92697, USA; kaderj@uci.edu, jukader@gmail.com

Space Telescope Science Institute, 3700 San Martin Drive, Baltimore, MD 21218, USA

Department of Physics and Astronomy, UCLA, 430 Portola Plaza, Box 951547, Los Angeles, CA 90095-1547, USA

Indiana University, University Information Technology Services, CIB 2709 E 10th Street, Bloomington, IN 47401 USA

Key Laboratory for Research in Galaxies and Cosmology, Shanghai University, 80 Nandan Road, Shanghai 200030, People's Republic of China

Department of Natural Sciences, University of Michigan-Dearborn, 4901 Evergreen Road, Dearborn, MI 48128, USA

Saint Martin's University, 5000 Abbey Way SE, Lacey, WA 98503, USA

Cerro Tololo Inter-American Observatory, NSF's National Optical-Infrared Astronomy Research Laboratory, Casilla 603, La Serena, Chile

Pentrum für Astronomie der Universität Heidelberg, Astronomisches Rechen-Institut, Mönchhofstraße 12, D-69120, Heidelberg, Germany

European Southern Observatory, Karl-Schwartzschild-Straße 2, D-85748 Garching bei München, Germany

Received 2022 April 25; revised 2023 March 22; accepted 2023 March 24; published 2023 June 15

Abstract

We present wide-field, high resolution maps of the color excess for 14 globular clusters toward the Southern Galactic bulge. The maps were derived using Gaia EDR3 astrometry and stellar photometry from the Blanco DECam Bulge Survey, which is a deep, wide-field ugrizY photometric survey of the southern Galactic bulge. Comparisons with WISE 12 μ m images of thermal continuum emission demonstrate that the maps presented here trace interstellar extinction by dust down to 5" scales. We use the reddening-corrected photometry of proper motion-selected cluster stars to build color–magnitude diagrams for the target globular clusters, which show residual broadening in excess of that expected from the photometric errors alone. This residual broadening is likely to be driven by star-to-star elemental abundance variations.

Unified Astronomy Thesaurus concepts: Globular star clusters (656); Broad band photometry (184); Interstellar dust extinction (837); Red giant branch (1368); Galactic bulge (2041)

1. Introduction

Photometric studies of globular clusters (GCs) at low Galactic latitudes are notoriously challenging thanks due to sample contamination by field stars and foreground reddening. Sightlines through the Galactic midplane will generally include stars from the Galactic disk population, which act as foreground contaminants in color-magnitude diagrams (CMDs). Additionally, given that GCs are partially transparent, images will include stars from the Galactic bulge population, which act as background contaminants in CMDs. Contamination by field stars can reduce the definition of cluster CMD sequences because their colors and magnitudes are generally inconsistent with those of cluster stars. Field crowding can also distort cluster CMD sequences to the degree that the image angular resolution is insufficient to separate individual stars. This effect that can be rather pronounced when considering the compact GCs toward the bulge, or even considering the high surface density bulge population stars by themselves.

Sightlines passing through the dusty Galactic midplane suffer from foreground reddening because interstellar dust preferentially attenuates and scatters shorter wavelengths. Much of the interstellar dust of the Galaxy is concentrated within the Galactic disk, so the reddening, E(B-V), is preferentially higher for lines of sight toward lower Galactic latitudes. The structure of the dusty ISM in the Galactic disk is

Original content from this work may be used under the terms of the Creative Commons Attribution 4.0 licence. Any further distribution of this work must maintain attribution to the author(s) and the title of the work, journal citation and DOI.

highly non-uniform and includes diffuse dust as well as dark nebulae, which span a wide variety in morphology, size, and density. Therefore, low Galactic latitude sightlines also have a preferentially higher degree of differential reddening, which serves to artificially increase the color dispersion of cluster CMD sequences (Gonzalez et al. 2011; Green et al. 2018; Chen et al. 2019; Surot et al. 2019).

Photometric studies of stellar populations toward the Galactic bulge are challenging given that they must overcome strong and spatially variable extinction, which can significantly affect NUV-optical measurements. Many studies have used the full-sky Galactic dust extinction maps of Schlegel et al. (1998), with the caveat that these become less reliable below |b| = 6and are at relatively low resolution (~few arcminutes). Maps of several inner bulge fields have been derived using NIR J, H, K_S photometry of RGB and AGB bulge stars. For example, Schultheis et al. (1999) used DENIS photometry to create a 20square-degree map of the inner Galactic bulge and Dutra et al. (2003) used 2MASS to create an extinction map within 10° of the Galactic center. Using the NIR photometry of bulge red clump (RC) stars from the Vista Variables in the Via Lactea (VVV; Minniti et al. 2010) survey, Gonzalez et al. (2011) generated extinction maps with a resolution of 3' in a large field toward the Galactic bulge $(-8^{\circ} < b < -0^{\circ}4, 0^{\circ}2 < l < 1^{\circ}7)$. Improving on this technique, Simion et al. (2017) used the NIR VVV photometry of RC stars to create a large-scale, 300 square degree map of the southern Galactic bulge with a resolution of 1'. Higher resolution extinction maps toward individual Galactic bulge GCs also exist (von Braun & Mateo 2001; Melbourne & Guhathakurta 2004; Alonso-García et al. 2012;

 Table 1

 Table of the Main Properties of the 14 Clusters in the Current Sample

Name	Alt. Name	R.A. _{J2000} ^a (deg)	Decl. _{J2000} ^a (deg)	$\mu_{\alpha}^{\bar{\mathbf{b}}}$ (mas yr ⁻¹)	(mas yr^{-1})	r _h ^a (arcmin)	m _V ^a (mag)	$M_{\rm V}^{\rm a}$ (mag)	$E(B-V)^{a}$ (mag)	R _{GC} ^a (kpc)	(Fe/H) ^a (dex)
NGC 6441		267.554	-37.051	-2.568	-5.322	0.57	7.15	-9.63	0.47	3.9	-0.46
NGC 6453		267.716	-34.599	0.165	-5.895	0.44	10.08	-7.22	0.64	3.7	-1.50
NGC 6528		271.207	-30.056	-2.327	-5.527	0.38	9.60	-6.57	0.54	0.6	-0.11
NGC 6540	Djorg 3	271.536	-27.765	-3.760	-2.799	0.9	9.30	-6.35	0.66	2.8	-1.35
NGC 6544		271.836	-24.997	-2.349	-18.557	1.21	7.77	-6.94	0.76	5.1	-1.40
NGC 6553		272.315	-25.908	0.246	-0.409	1.03	8.06	-7.77	0.63	2.2	-0.18
NGC 6569		273.412	-31.826	-4.109	-7.267	0.8	8.55	-8.28	0.53	3.1	-0.76
NGC 6624		275.919	-30.361	0.099	-6.904	0.82	7.87	-7.49	0.28	1.2	-0.44
NGC 6626	M28	276.137	-24.870	-0.301	-8.913	1.97	6.79	-8.16	0.40	2.7	-1.32
NGC 6637	M69	277.846	-32.348	-5.113	-5.813	0.84	7.64	-7.64	0.18	1.7	-0.64
NGC 6638		277.734	-25.496	-2.550	-4.075	0.51	9.02	-7.12	0.41	2.2	-0.95
NGC 6642		277.976	-23.476	-0.189	-3.898	0.73	9.13	-6.66	0.40	1.7	-1.26
NGC 6652		278.940	-32.991	4.750	-4.450	0.48	8.62	-6.66	0.09	2.7	-0.81
NGC 6656	M22	279.100	-23.905	9.833	-5.557	3.36	5.10	-8.50	0.34	4.9	-1.70

Notes.

Kunder et al. 2013; Cohen et al. 2014; Surot et al. 2019). However, there are no homogeneous sets of sub-arcminute extinction maps for the GCs that are targeted in our program.

In this study, we aimed to construct accurate, high resolution, wide-field reddening maps of a large sample of GCs toward the Galactic bulge. We leveraged deep, high resolution NUV-optical-NIR ground-based photometry and proper motions from Gaia EDR3 (Gaia Collaboration et al. 2018, 2021) to reliably select cluster member stars, from which maps of interstellar reddening were constructed. We focused on nonparametric methods to build the maps without relying on physical models of the GCs, which can have ambiguous interpretations. The reddening maps were used to correct the photometry of the cluster stars, which were used to produce cluster CMDs that show improved definition in the cluster sequences. They also reveal that the red giant branches (RGBs) of the clusters in g versus g - i, or r versus u - rdiagrams are either broader than expected from photometric errors alone or are split, which are indications of light element chemical variations in the atmospheres of the cluster stars. This paper is organized as follows: in Section 2 we describe our photometric data set, photometric measurement errors, and ancillary data. In Section 3, we describe our GC sample selection. In Section 4, we give a detailed explanation of our method to create the reddening maps and correct the cluster photometry. In Section 5, we present our reddening maps and the cluster CMDs made from corrected photometry. In Section 6, we compare the structure of the maps with literature maps and archival multiwavelength data. Finally, we provide our concluding remarks in Section 7.

2. Observations and Data

The Blanco Dark Energy Camera (DECam) Bulge Survey (BDBS; Johnson et al. 2020; Rich et al. 2020) is a deep, sixband near-ultraviolet (NUV)-optical-near-infrared (NIR), and wide-field photometric survey of the southern Galactic bulge. Here, we summarize the key features of the survey and the photometric point-source catalog. Details regarding observations, image processing, data reduction, and photometric calibrations can be found in Johnson et al. (2020).

The image data were collected with the wide-field DECam imager on the Blanco 4 m Telescope at the Cerro Telolo

International Observatory during 2013 June 1–5, 2013 July 14–15, and 2014 July 14–21. Images were taken through the NUV-optical-NIR ugrizY passbands and cover more than 200 square degrees of the southern Galactic bulge $(-11^{\circ} < l < 11^{\circ}, -2^{\circ} < b < -9^{\circ},$ and down to b=-13 along the Galactic minor axis). Typical seeing in the u band was 0.8–1.9.2. The photometric point-source catalog contains 250 million unique sources, with median 5σ depths of 23.5, 23.8, 23.5, 23.1, 22.5, and 21.8 mag in the ugrizY filters. The BDBS catalog was cross-matched with Gaia EDR3 to ensure that we could use proper motions to select cluster stars (Marchetti et al. 2022). About 40% of the BDBS point sources in each cluster field had a Gaia EDR3 match, although this figure varies between 21% and 78% depending on the cluster.

3. Globular Cluster Sample

There are 26 known GCs toward the Galactic bulge that fall inside the BDBS footprint. In this paper, we focus on the 14 most massive ($M_V < -6.35$ mag) of these clusters. We list their main properties in Table 1. The remainder of the clusters are poorly populated or at very low Galactic latitudes, and reddening maps for their fields could not be constructed using the methods of this paper without introducing substantial inhomogeneities in our analysis. Most of the clusters in our sample belong to the Galactic bulge population of GCs according to the recent chemodynamical study of Massari et al. (2019). NGC 6441, NGC 6453, and NGC 6544 were found to be part of a low energy system that could not be associated with any known merger event, while NGC 6656 was found to be a main disk GC passing in front of the bulge. Therefore, 10 of the 14 clusters in our sample are likely to be bulge members, three are of indeterminate origin, and one belongs to the main disk population. The positions and sizes of the sample clusters are indicated as white circles superimposed on the Galactic extinction map shown in Figure 1.

4. Analysis

In this section, we discuss the steps taken to identify cluster members, build ridge lines to fit the cluster sequence in the

^a Values collected from Harris (1996).

^b Values from Vasiliev (2019).

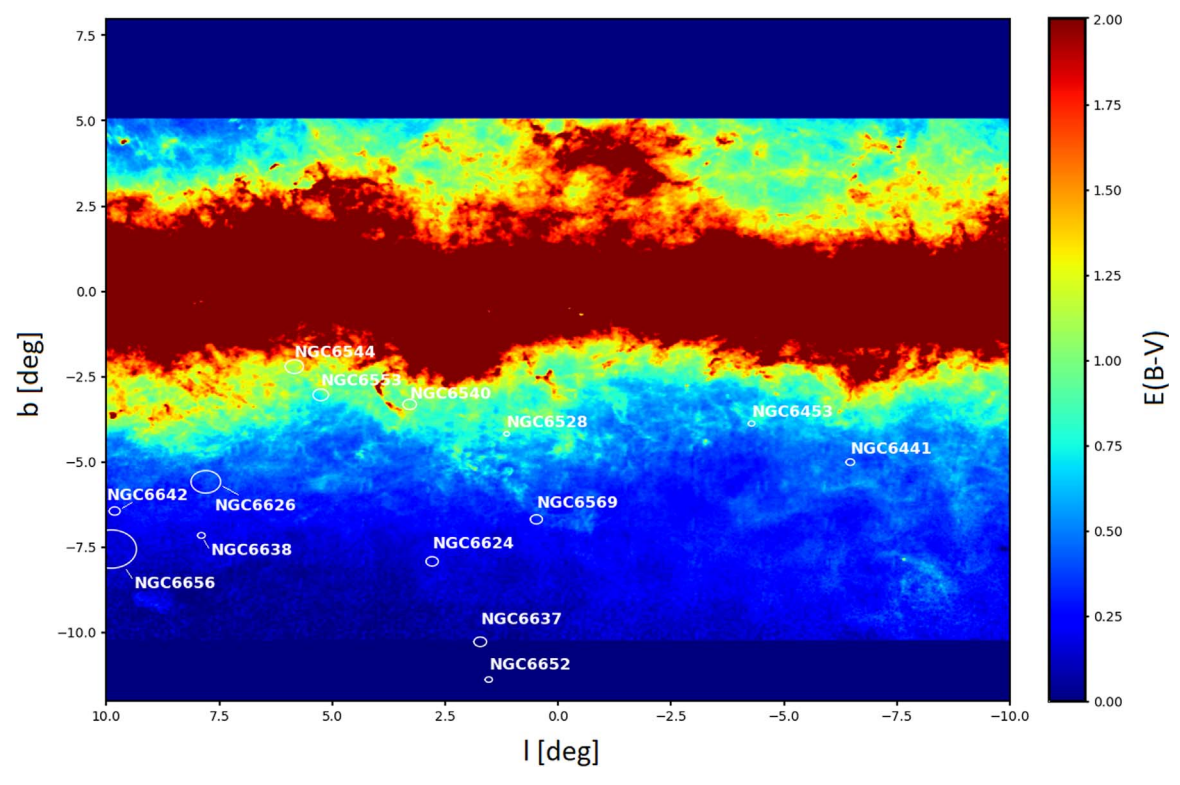


Figure 1. Map of the E(B-V) color excess including much of the BDBS footprint, adapted from the A_u map from Simion et al. (2017). The positions of the sample GCs are indicated with white circles. The radius of each circle is equal to 10 times the half-light radius $(10 \times r_h)$ of the cluster. The resolution of the map is $1' \times 1'$. The map covers a large portion of the Galactic bulge ($|l| < 10^\circ$; $-10^\circ < b < +5^\circ$), containing much of the BDBS footprint, but excludes all or parts of NGC 6652, and NGC 6656. The 14 target clusters span Galactic latitudes from $b = 11^\circ$.4 to $b = -2^\circ$.2. The clusters at higher galactic latitude are less affected by interstellar extinction. The BDBS footprint contains more than 25 GCs in total.

CMDs, develop the final reddening maps, and correct the photometry.

4.1. Identifying Cluster Members

We use Gaia EDR3 proper motions (PMs) to minimize the contribution of non-cluster field stars in the creation of the reddening maps because these stars are generally at different distances along the line of sight and their inclusion would produce erroneous reddening corrections for bona fide cluster stars. Vector point diagrams of the PMs of stars within 10 r_h of each cluster were used to distinguish between field stars and cluster members. The distribution of points in $\mu_{\alpha} \cos(\delta)$ versus μ_{δ} space were fitted with Gaussian mixture models in both directions. For all clusters, we found a Gaussian component in both $\mu_{\alpha} \cos(\delta)$ and $\mu\delta$ that was consistent with the mean system PMs from Vasiliev (2019). We define r_{PM} for each cluster, which is $2\times$ the mean of the Gaussian σ values of the cluster $\mu_{\alpha} \cos(\delta)$ and μ_{δ} distributions, where the centroid is from Vasiliev (2019). We find that the average proper motion radius for our sample is $r_{\rm PM} = 1.24 \pm 0.839 \, {\rm mas \ yr^{-1}}$. In selecting cluster members, we opt for a selection threshold of $r_{\text{select}} = 1 \text{ mas yr}^{-1}$, except for NGC 6544 where we use $r_{\text{select}} = 3 \text{ mas yr}^{-1}$ because it has a PM distribution that is clearly offset from the bulge star distribution.

4.2. Building the Ridge Lines

Our goal was to build a ridge line to fit the MS-RGB sequence for our target GCs without relying on isochrone models, which depend on assumptions about the physical conditions of the cluster. The faint limit of our survey is roughly 22 mag in r and g bands. Therefore, depending on the

distance to a cluster, the MS stars are potentially below our detection limit and are not included. In such cases, the ridge line is only fitted to the RGB. All steps include the use of cluster member stars only. The first step in building the ridge lines was to select stars within $1-4 r_h$. The HB tends to skew the ridge line fit away from the RGB, so we visually identified HB stars and removed them in all clusters before continuing with the ridge line fit. Blue HB stars clearly separate from the RGB in u-r and g-i CMDs, and are easily identified and removed. Meanwhile, red HB stars typically intersect the RGB, and in such cases we clip the RGB within ~ 0.5 mag of the intersection. We divided the cluster stars into magnitude bins of 0.25 mag, and in each bin computed the probability-weighted median color. Membership probability was parameterized as the reciprocal of the distance from the cluster mean PM coordinates in $\mu_{\alpha} \cos(\delta)$ versus μ_{δ} space, normalized to r_{select} . After the probability-weighted color is found, we use sigma clipping with a 2σ rejection to eliminate outliers and then recompute the probability-weighted median color. We iterate this process in each magnitude bin until the process converges. We reduce noise in the color direction of the resulting ridge line using univariate spline interpolation with a smoothing factor that was chosen by hand for each cluster to best reduce noise while not over-smoothing. The process is carried out in both colors for each cluster. The final ridge lines, overlaid on the uncorrected CMDs, can be seen in Figures 2 and 3.

4.3. Sampling the Color Excess

With the smoothed ridge line fit to the cluster CMDs in hand, we are able to compute the color excess of the individual cluster stars. We choose to compute the color excess only for

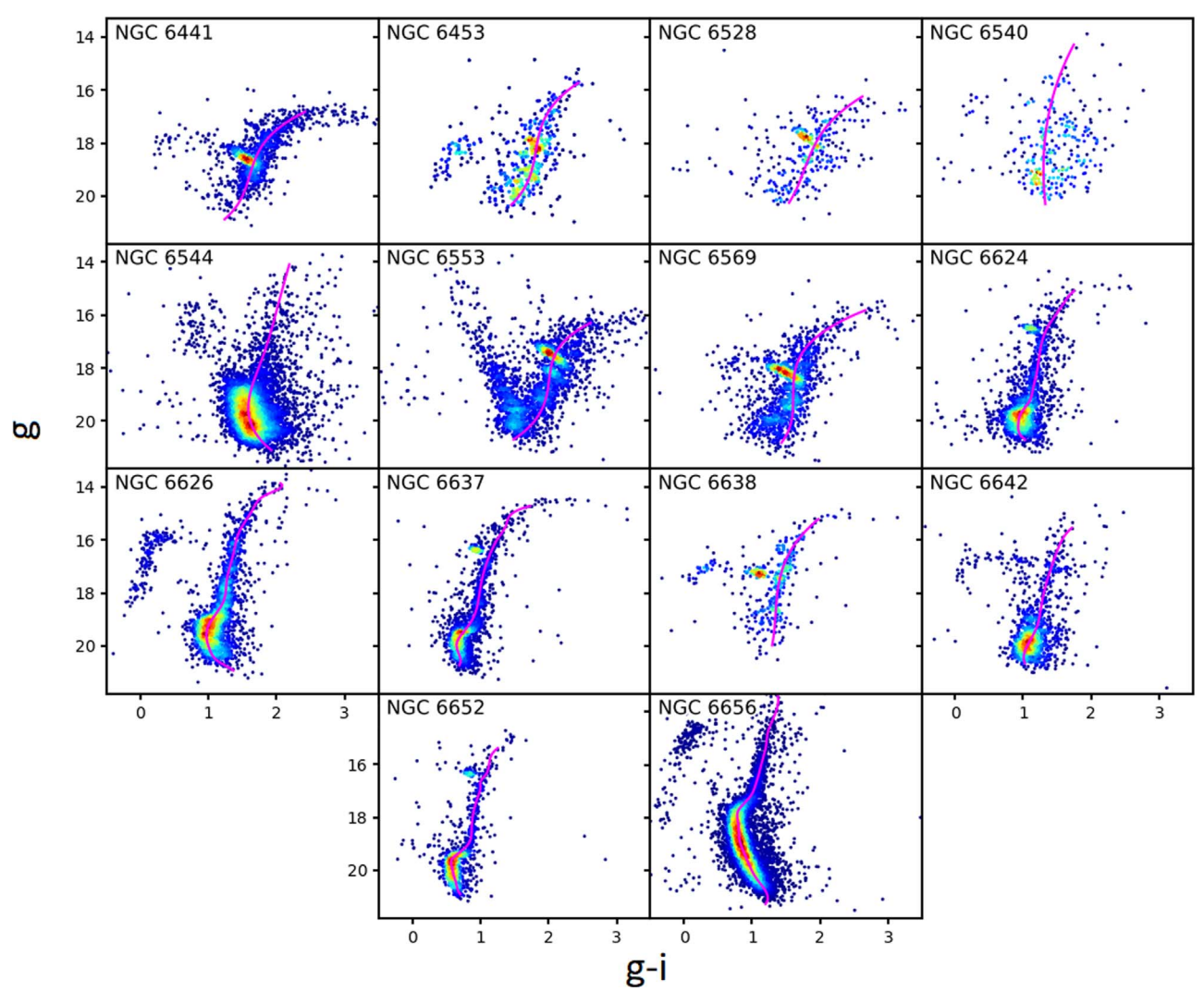


Figure 2. Here we present the g vs. g-i CMDs for proper motion-selected members within 10 r_h of the cluster centers, not yet corrected for reddening. The stars are colored according to the number of neighbors within a circular radius of k=0.1 mag to show the relative density of points on the CMD. For each cluster, we fit a ridge line to the stars near the cluster center, excluding HB stars. The ridge lines are shown in magenta.

stars falling within ~ 0.5 mag of the ridge line in the color direction as an added assurance that the reddening map is constructed with a minimum contamination from non-cluster field stars. Following Alonso-García et al. (2012), we move each star along the reddening vector until it intersects the ridge line, as illustrated in Figure 4. The resulting vertical (brightness) and horizontal (color) displacements are assumed to be due to interstellar extinction (A_g or A_r), reddening (E(g-i)) or E(u-r)), and to photometric errors.

The primary contributions to the uncertainty in the derived extinction are the photometric measurement errors in u, g, r, and i. To estimate the errors σ_{A_g} and σ_{A_r} , we follow Alonso-García et al. (2012) in constructing an error ellipse for each star used in the analysis. We compute the error ellipse for each star using the measurement error in its color, σ_c and magnitude σ_m . The error ellipse is tilted because the errors in magnitude and color are correlated. The angle of the tilt is defined using the covariance of the measured color and magnitude, σ_{cm} :

$$\tan(2\theta) = \frac{2\sigma_{\rm cm}}{\sigma_{\rm c}^2 + \sigma_{\rm m}^2}.$$
 (1)

The covariance is defined as

$$\sigma_{\rm cm} = \rho_{\rm cm} \sigma_{\rm c} \sigma_{\rm m}, \qquad (2)$$

where ρ_{cm} is the Pearson rank correlation coefficient computed from the ensemble of color and magnitude errors across all of the stars in the cluster. The semimajor and semiminor axis lengths of the error ellipse are defined in the following way:

$$\sigma_{c'}^2 = \frac{\sigma_c^2 + \sigma_m^2}{2} + \left[\frac{(\sigma_c^2 - \sigma_m^2)^2}{4} + \sigma_{cm}^2 \right]^{1/2}$$
 (3)

$$\sigma_{\rm m'}^2 = \frac{\sigma_{\rm c}^2 + \sigma_{\rm m}^2}{2} - \left[\frac{(\sigma_{\rm c}^2 - \sigma_{\rm m}^2)^2}{4} + \sigma_{\rm cm}^2 \right]^{1/2}.$$
 (4)

The error in the shift of the star to the ridge line is defined using the points of first and last contact between the ellipse and the ridge line, which is depicted schematically in Figure 4. Following a similar approach to that of Alonso-Garcia et al. (2011; Equation (27)), these points of contact define the error in

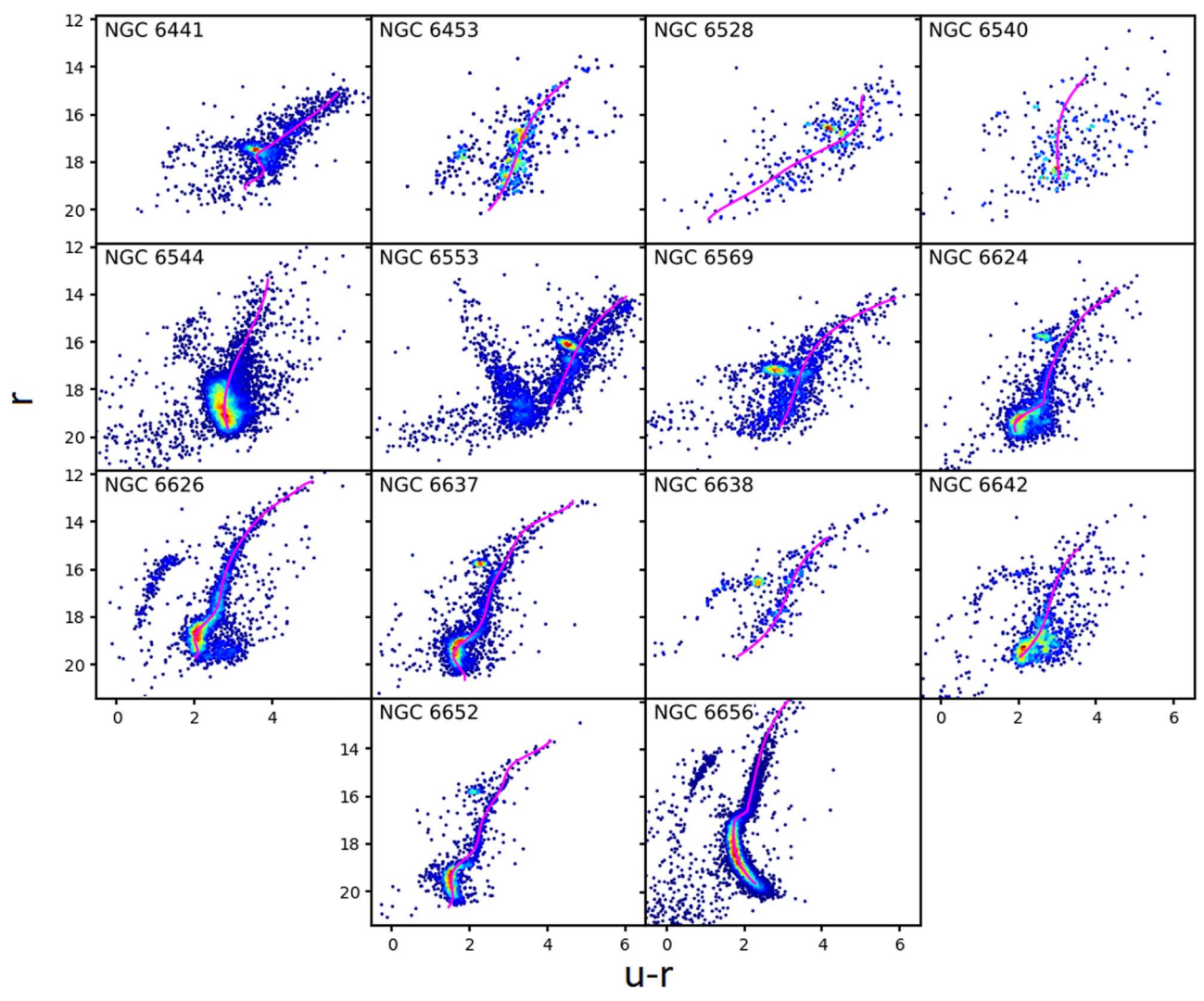


Figure 3. Similar to Figure 2 but in the r vs. u - r plane. Ridge lines fitted to inner cluster stars are shown here in magenta, overlaid on the CMD of all cluster member stars within $10 r_h$.

the shift (total extinction) as

$$\sigma_{A_{\text{mag}}} = \sigma_{\text{ellipse}} = 0.5 |\text{pfc} - \text{plc}|.$$
 (5)

The reddening vectors for each of the two CMD planes are directly related to the total-to-selective extinction described by the relations $A_g = R_{g-i}E(g-i)$ and $A_r = R_{u-r}E(u-r)$. The value of the total-to-selective extinction, R_{a-b} , gives the slope of the reddening vector. Using the definition of the color excess, $E(a-b) \equiv A_a - A_b$, the total-to-selective extinction can be computed as $R_{a-b} = A_a/(A_a - A_b)$. The total extinctions used to compute our reddening vectors, normalized to the B-V color excess, are:

$$A_u = 4.239E(B - V), (6)$$

$$A_g = 3.384E(B - V), (7)$$

$$A_r = 2.483E(B - V), (8)$$

$$A_i = 1.838E(B - V), (9)$$

from Green et al. (2018) for g, r, i and from Schlafly & Finkbeiner (2011) for u band, all derived using a $R_V = 3.1$ extinction law from Fitzpatrick (1999). The reddening vector

slopes were then computed as

$$R_{g-i} = \frac{A_g}{E(g-i)} = \frac{3.384}{3.384 - 1.838},\tag{10}$$

$$R_{u-r} = \frac{A_r}{E(u-r)} = \frac{2.483}{4.239 - 2.483}.$$
 (11)

From the shift of each star toward the ridge line, we derive a value of A_g or A_r , which are the extinctions of the stars relative to the empirical ridge line. From these, we compute the differential color excess $\Delta E(B-V)$ using Equations (7) and (8). Since the ridge lines are constructed from observed, reddened photometry, the color excess $\Delta E(B-V)$ derived using this method is relative to the average color excess of the of the clusters $\langle E(B-V) \rangle$, which is given in Table 1 for each target cluster. Thus, the estimated absolute color excess of the *i*th star is given by $E(B-V)_i = \Delta E(B-V)_i + \langle E(B-V) \rangle$.

4.4. Constructing the Extinction Maps

To find the color excess for the other cluster stars, it was necessary to estimate E(B-V) as a continuous function of the coordinates R.A. and decl. within the 10 r_h field of each cluster. We required a technique that would characterize E(B-V) as a

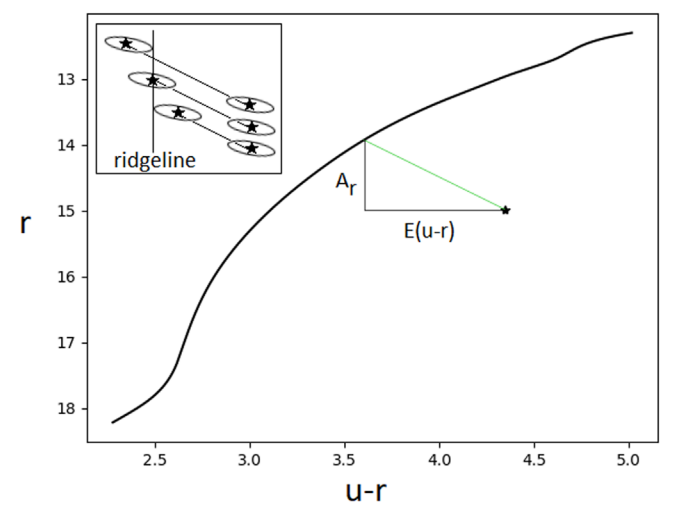


Figure 4. Schematic illustration of the procedure to compute extinctions for cluster stars using the fitted ridge lines. The main panel shows the r vs. u-r ridge line fitted to the SGB and RGB of NGC 6637 as a black curve. The green line, parallel to the reddening vector, connects the star to its predicted true position on the CMD. The extinction for the star, A_r , is the vertical displacement from the predicted true position. The inset shows how the error ellipse is used to compute σ_{ellipse} using the points of first and last contact between the ellipse and the ridge line.

smooth and continuous bivariate function of the spatial coordinates. We then fitted this function to the discretely sampled points, $E(B-V)_i$, weighted by the uncertainty in the measured color excesses, $\sigma_{\text{ellipse},i}$.

We used Gaussian process regression (GPR), which is a nonparametric, Bayesian technique to infer an underlying distribution by fitting a kernel-based probabilistic model to the observations. To compute the regression, we used the Python machine learning library scikit-learn (Buitinck et al. 2013), which offers an efficient GPR package. Instead of computing the probability distribution over the parameters of a specific function as in Bayesian linear regression, GPR computes the (prior) probability distribution over all possible functions that fit the data. Which functions are likely to be sampled in the Gaussian process (i.e., the prior distribution) depends on the choice of kernel, $\mathcal{K}(x, x'|\tau)$. The kernel specifies the covariance of E(B-V) at points x and x' as a function of the distance between them in a way that can be tuned using the hyperparameters τ . We chose to use the rational quadratic kernel (RQK),

$$\mathcal{K}(\mathbf{x}, \mathbf{x}') = \left(1 + \frac{d(\mathbf{x}, \mathbf{x}')^2}{2\alpha\ell^2}\right)^{-\alpha},\tag{12}$$

where d is the Euclidean distance between x and x', and the hyperparameters ℓ and α are the characteristic length scale and the scale mixture parameter, respectively. In our application, ℓ is a scalar because we do not assume anisotropy in the distribution of stars on the sky and was fixed to the minimum on-sky angular separation of the sampled RGB stars for each cluster. The hyperparameter α makes the RQK equivalent to adding together many radial basis function kernels with different length scales and was appropriate here because we expect differential reddening fluctuations to be present across many length scales. For a rational quadratic kernel with hyperparameter values equal to those typically found in our study (length scale of order $\ell=1''$ and scale mixture parameter

 $\alpha = 2 \times 10^{-4}$; see Table 2), sample functions drawn from the prior show fluctuations of up to ~ 0.25 mag over several arcminutes and fluctuations of up to ~ 0.1 mag over several arcseconds. These functions are suitable for reconstructing the color excess image, which can generally be expected to simultaneously vary across several spatial frequencies.

The fundamental assumption of the Gaussian process is that the observations y and the true underlying function outputs f^* are distributed as an (N+M)-dimensional multivariate normal, where N is the number of observations and M is the number of unobserved locations x^* , where an estimate of the underlying function is sought. The posterior distribution over function space is calculated from the prior and the observed data using the Bayes Rule. Predictions for the value E(B-V) at arbitrary, unobserved positions are calculated by integrating all possible predictions for that position by the posterior distribution, which is a tractable operation due to the fundamental multivariate normal assumption. The kernel hyperparameters τ are tuned by maximizing the log likelihood of the observed data. The $20r_h \times 20r_h$ field around each cluster is divided into a square grid of $5'' \times 5''$ cells onto which the GPR estimated the value of E(B-V). Cells containing observed data took on E(B-V)values equal or similar to the observation, depending on the observation uncertainty.

5. Results

In this section, we present the reddening maps and describe their appearance. We define the variation in color excess across each field, $\delta E(B-V)$, as the 6σ range $(\pm 3\sigma)$ in the distribution of $\Delta E(B-V)$ from our final maps. The maps for each sample cluster are presented alongside the uncorrected and differential reddening-corrected CMDs in Figures 5–18. We also describe differences and similarities between our derived maps and the VVV-derived maps from Simion et al. (2017), where available. Our maps are presented alongside the Simion et al. (2017) maps in the Appendix. We describe the morphology of the maps with respect to known structures of absorbing material along the line of sight. The CMDs of cluster stars using dereddened photometry are presented in this section and are compared with CMDs of cluster stars using uncorrected photometry in Section 6.

We compile the derived color excess variations (differential reddening) and GPR optimized hyperparameters in Table 2. The derived color excess variations ranged from 0.042 (NGC 6642) to 0.350 (NGC 6544), with a median of 0.90 \pm 0.077. We find a statistically significant positive correlation between differential reddening $\delta E(B-V)$ and the average (zero-point) color excess of the cluster from Harris (1996), with a Pearson rank correlation coefficient of r=0.64, P=0.014. This correlation is not unexpected and is a reflection of the clumpy nature of the cold ISM toward the bulge.

5.1. NGC 6441 (Figure 5)

NGC 6441 is a very metal-rich, massive Galactic bulge GC. Harris (1996) gives a metallicity of [Fe/H] = -0.46, while Gratton et al. (2007) find [Fe/H] = -0.34. The average reddening across the field of NGC 6441 is E(B-V) = 0.47 (Harris 1996). From our 11'.4 × 11'.4 map centered on NGC 6441, we find that the color excess variations are significant, with $\delta E(B-V) = 0.165$. There is a general trend of increasing extinction from west to east across the field, and the southern

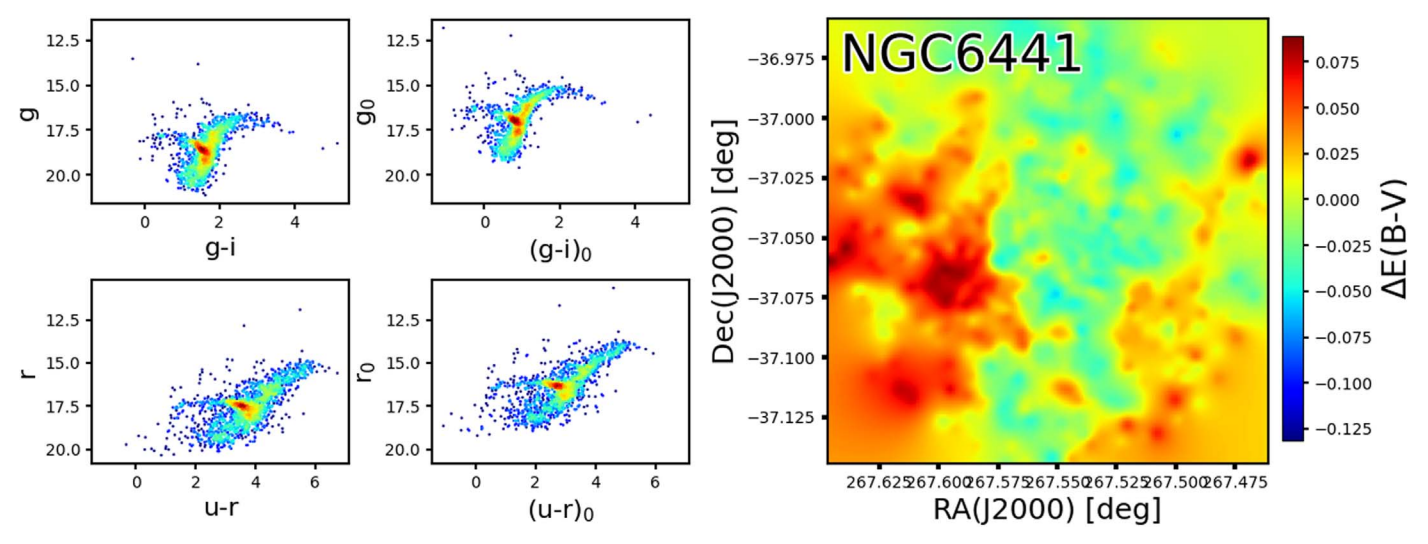


Figure 5. The right-hand panel shows the differential reddening map for NGC 6441, scaled linearly between -5σ and $+3\sigma$ of the zero-point color excess, $E(B-V)_0$. North is up and east is left. The left-hand panels show the g vs. g-i (top) and r vs. u-r (bottom) CMDs of the cluster before and after correcting for differential reddening. Each star is color-coded according to the number of neighbors within a circular radius k=0.1 mag on the CMD plane. The color-coding is scaled logarithmically. The RGB is more narrow and dense after applying the differential reddening correction.

 Table 2

 Table of Gaussian Process Regression Parameters Used to Reconstruct the Color Excess as a Function of R.A. and Decl. in Both Color Spaces for All Clusters

Cluster	$\delta E(B-V)$	g versus $g-iLength Scale (")$	alpha	r versus $u-rLength Scale (")$	alpha
NGC6441	0.165	0.76	0.00039	0.76	0.00057
NGC6453	0.127	1.05	0.00020	1.84	0.00020
NGC6528	0.150	1.93	0.00052	1.93	0.00091
NGC6540	0.074	3.07	0.00031	3.64	0.00028
NGC6544	0.350	0.86	0.00048	0.90	0.00028
NGC6553	0.088	1.37	0.00015	1.43	0.00024
NGC6569	0.120	1.67	0.00032	1.37	0.00197
NGC6624	0.070	0.98	0.00010	0.98	0.00009
NGC6626	0.134	1.09	0.00021	1.18	0.00011
NGC6637	0.042	1.07	0.00003	1.07	0.00012
NGC6638	0.064	1.20	0.00019	2.35	0.00017
NGC6642	0.046	1.10	0.00008	1.10	0.00005
NGC6652	0.042	1.15	0.00004	1.33	0.00010
NGC6656	0.091	1.18	0.00016	1.28	0.00001

part of the field has more extinction than the northern part. The higher extinction in the eastern part of the map may be associated with the Galactic dark cloud FEST 1–410 (Dutra & Bica 2002).

The improvement in the CMD is most pronounced for the RGB stars, which have a noticeably smaller dispersion in both g-i and u-r colors. As noted by Busso et al. (2007) and Rich et al. (1997), this cluster has a prominent red HB, characteristic of metal-rich GCs, which is tilted. There is also a blue HB component, which forms a long tail, both of which were excluded when creating our reddening map. However, the morphology of the HB is preserved after applying the reddening corrections, which suggests that the RHB tilt is not due to differential reddening effects.

5.2. NGC 6453 (Figure 6)

NGC 6453 is an intermediate mass, low-metallicity, post-collapse GC in the Galactic bulge (Ortolani et al. 1999). The metallicity of the cluster is given as [Fe/H] = -1.50 by Harris (1996). NGC 6453 is a distant cluster, which located 8.5 kpc

from the Sun (Valenti et al. 2010) and 3.7 kpc from the Galactic center (Harris 1996). The mean reddening toward this cluster is given as E(B-V)=0.64 by Harris (1996), and was found to be as high as 0.7 by Ortolani et al. (1999). From our 8'. 8 × 8'. 8 reddening map centered on NGC 6453, we find that the color excess variations across the extended field of NGC 6453 are moderate, with $\delta E(B-V)=0.127$. The most striking feature of the map is a wide filament of foreground extincting material that enters the field from the northwest and continues down to the core of the cluster, where it terminates. The color excess along the filament is 0.02–0.04 mag above the zero-point. This structure may represent one of the southern tendrils of the dark cloud Barnard 283 (Barnard et al. 1927). The rest of the field is relatively free from variations in extinction relative to the zero-point.

The improvement in the cluster CMD is significant. The color dispersions of the RGB and HB components are both visually decreased and the distinction between the two components becomes more pronounced after the reddening corrections. Because of the large distance to this cluster

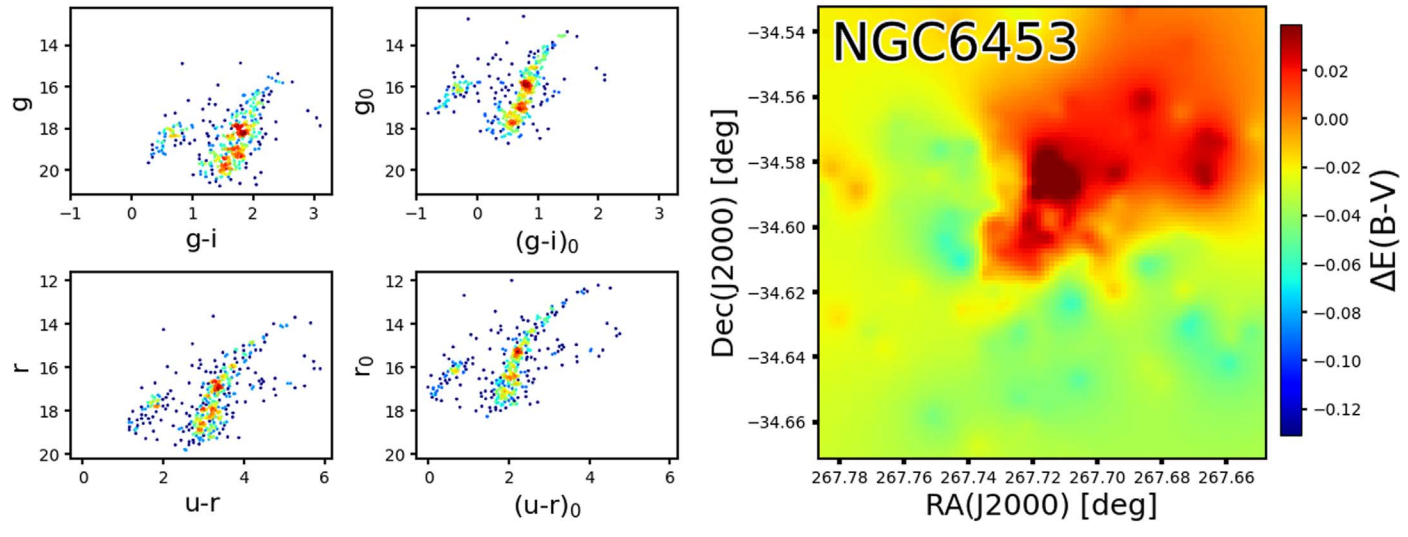


Figure 6. Same as in Figure 5 but for NGC 6453.

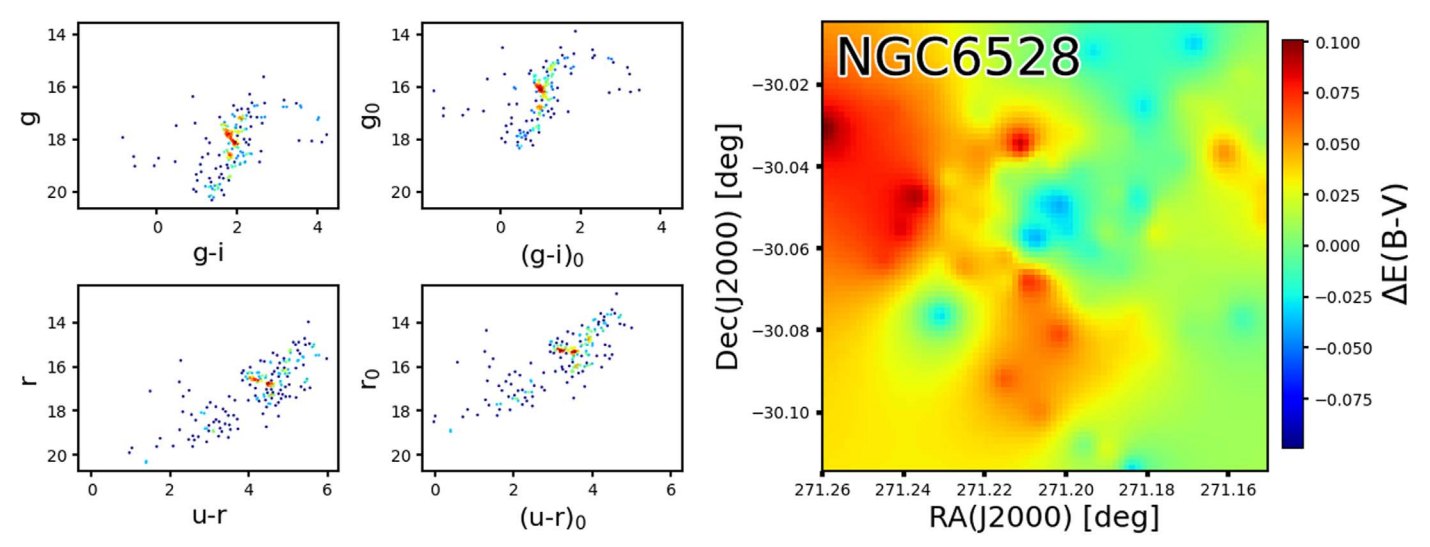


Figure 7. Same as in Figure 5 but for NGC 6528.

 $(d_{\odot} = 10.7 \text{ kpc}; \text{ Valenti et al. 2010})$, the cluster CMD is shallow and does not reach past the base of the RGB.

5.3. NGC 6528 (Figure 7)

NGC 6528 was studied extensively by Calamida et al. (2014), who combined ground-based Strömgen and NIR photometry with Hubble Space Telescope-based proper motions to correct their CMDs for differential reddening. NGC 6528 is an extremely metal-rich GC ([Fe/H] = -0.11, Harris 1996). The cluster is located at a distance of $d_{\odot} = 7.6$ kpc (Harris 1996), which places it very close to the Galactic center. Along with NGC 6553, which has similarly high metallicity, this cluster is in Baade's window and thus has comparatively little extinction for a GC near the Galactic center (Carretta et al. 2001). Across the 7.6×7.6 field centered on NGC 6528, we find color excess fluctuations of $\delta E(B)$ -V) = 0.150. The heaviest extinction is toward the east and south of the field, which corresponds to the projected positions of the LDN 41 (Lynds 1962) and Barnard 298 dark nebulae, respectively. The color excess in these two portions of the map is ~ 0.07 mag above the literature mean E(B-V) for NGC

6528. The northwestern part of the map is mostly free from variations in E(B-V).

The cluster CMD is visibly improved after applying the reddening corrections using the E(B-V) map. The RGB and red clump are more pronounced and the color dispersion of both features is noticeably reduced. Our CMDs reach down to the base of the RGB ($g_0 \sim 18.25$) and up to the TRGB. Our g, i CMDs reveal a possibly curved RGB, where the TRGB terminates at the same g as the HB. This feature has been noted elsewhere and is probably due to blanketing in this very metal-rich cluster (Richtler et al. 1998).

5.4. NGC 6540 (Figure 8)

NGC 6540 (Djorg 3) is a compact cluster that is located toward the Galactic bulge, with literature distances varying between $d_{\odot} = 3-5.3$ kpc. The Harris (1996) [Fe/H] value for the cluster is -1.35 but literature estimates tend to vary considerably between -1.01 and -1.5 (Vulic et al. 2018; Geisler et al. 2021). NGC 6540 was assumed to be an open cluster until Bica et al. (1994) confirmed its identity as a GC, with an extended blue HB. The Harris (1996) color excess is

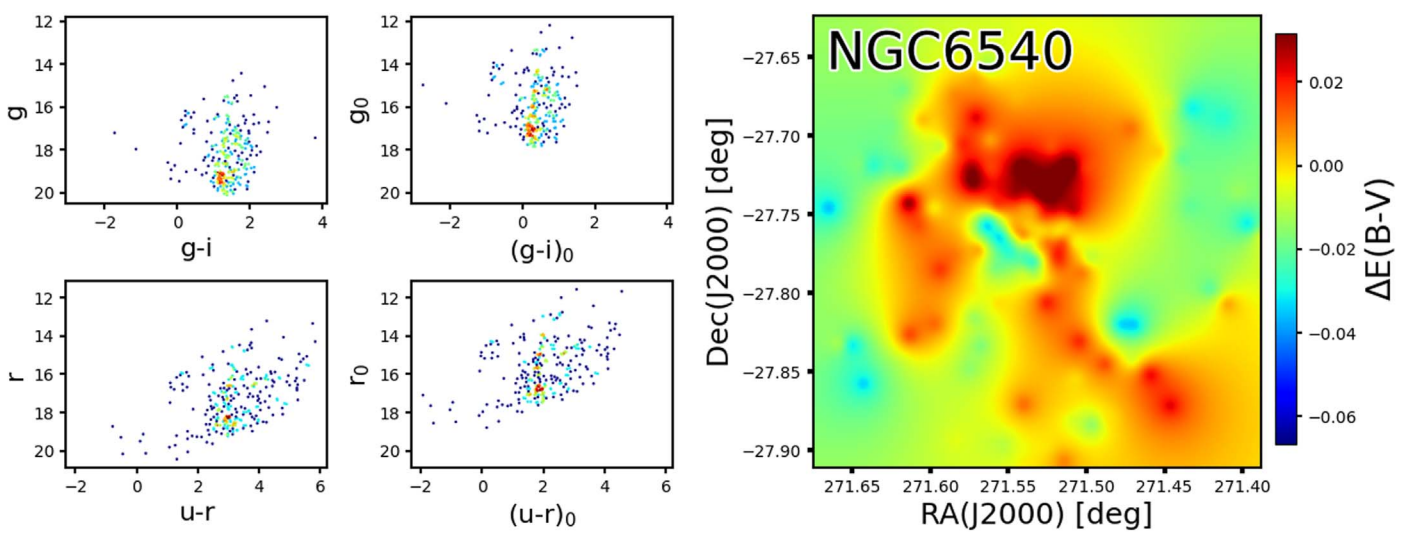


Figure 8. Same as in Figure 5 but for NGC 6540.

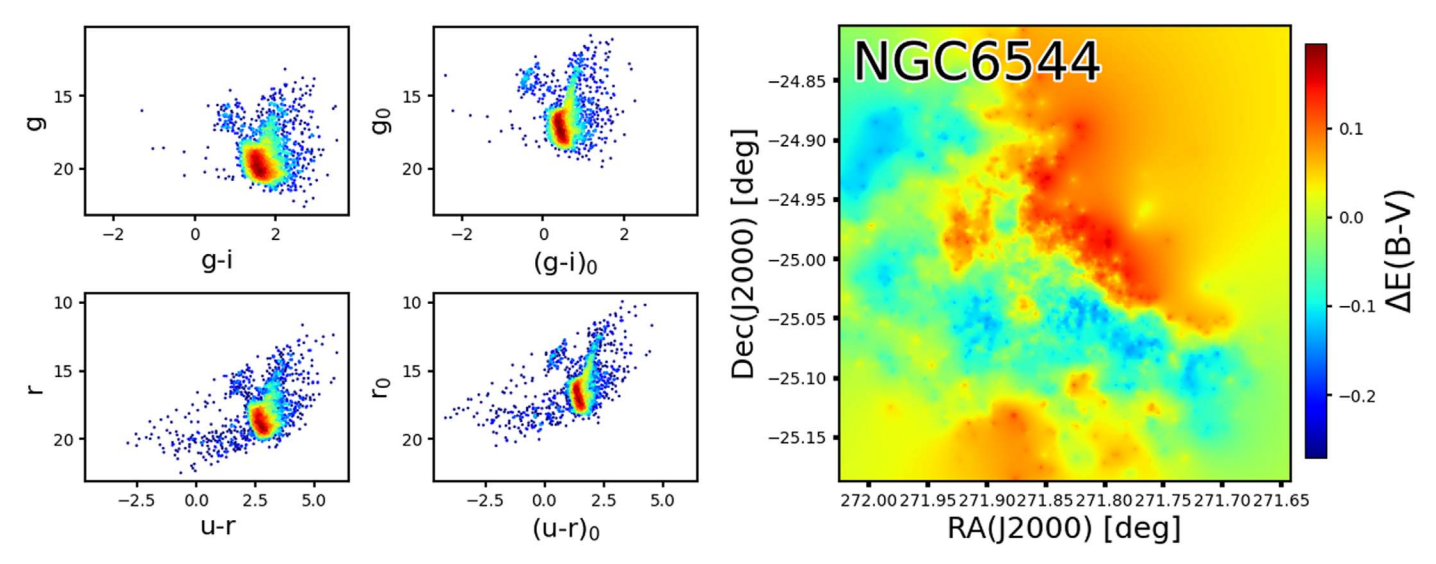


Figure 9. Same as in Figure 5 but for NGC 6544. This map is scaled between $-5\sigma_{E(B-V)}$ and $+3\sigma_{E(B-V)}$.

quoted at E(B-V) = 0.66, and Bica et al. (1994) give a consistent estimate of E(B-V) = 0.7 using the red edge of the blue HB from their V versus B-V CMDs. Our analysis reveals color excess variations on the order $\delta E(B-V) = 0.074$ across the $18' \times 18'$ field centered on the cluster. The most striking feature in the reddening map is the large $\Delta E(B-V)$ across a large portion of the northern field. The large color excess in the north part of the field corresponds with the projected position of the filamentary dark nebula LDN 116, which passes in the E-W direction across the northern edge of the $10 \ r_h$ field of NGC 6540.

Our reddening-corrected CMDs enhance the distinctions between cluster sequences and bulge/disk field sequences. In the g, i diagram, the cluster RGB has its base near $g_0 = 16$, $(g - i)_0 = 0.1$, and extends up to $g_0 = 12$. The blue HB is also easily identified at $g_0 = 14$, $(g - i)_0 = -1$. Although we have used a PM cut to reduce field star contamination, the bulge red HB is still evident at $g_0 = 15$, $(g - i)_0 = 0.9$. The disk main sequence, bulge evolutionary sequence, and possibly fainter cluster stars intersect below $g_0 = 16.5$.

5.5. NGC 6544 (Figure 9)

NGC 6544 is a relatively metal-poor GC with [Fe/ H = -1.4 from Harris (1996). Gran et al. (2021) find a consistent metallicity at [Fe/H] = -1.44 but also present evidence of [Fe/H] spreads larger than expected based on measurement errors. The cluster is at a projected distance of ~6 kpc from the Galactic center and is relatively nearby, with $d_{\odot} = 2.5$ kpc (Cohen et al. 2014). Based on orbital reconstructions from Contreras Ramos et al. (2017), Pérez-Villegas et al. (2020), and Massari et al. (2019), and clear observational signs of tidal disruption, NGC 6544 is thought to be an interloper passing through the main disk, projected against the bulge, which probably originated in the Galactic halo. It has been noted elsewhere that NGC 6544 suffers from significant differential reddening on small spatial scales (Cohen et al. 2014; Contreras Ramos et al. 2017). Indeed, our reddening map of the $24' \times 24'$ field centered on the cluster reveals fluctuations in color excess of $\delta E(B-V) = 0.350$. Most apparent is the large extinction in the northwestern half of

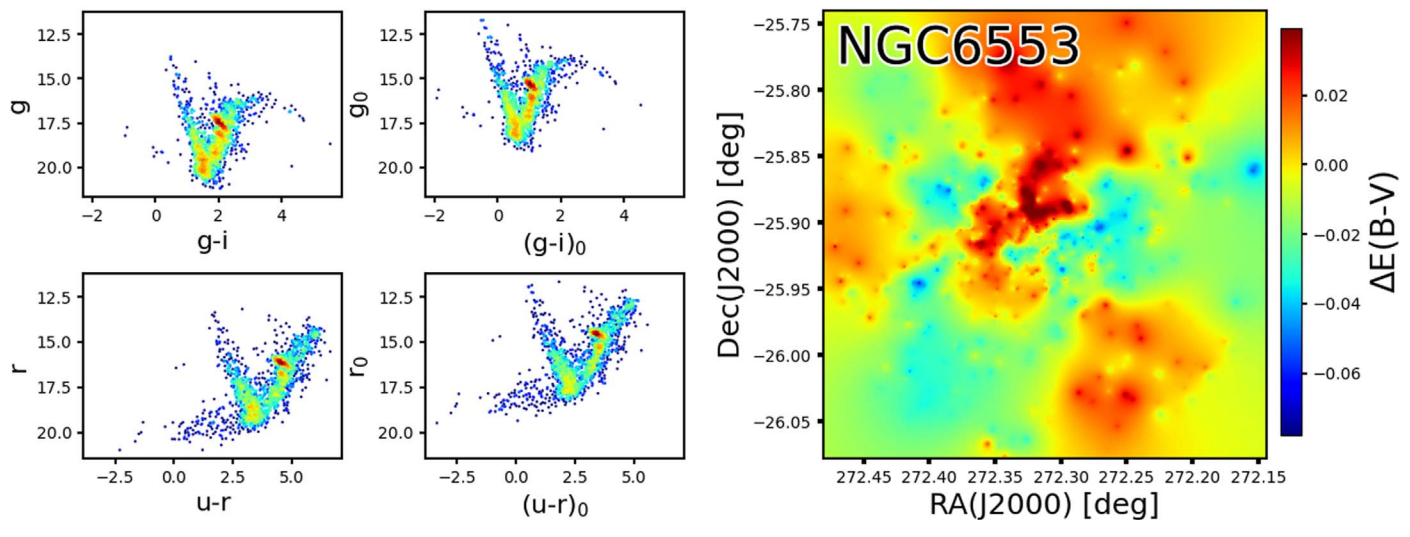


Figure 10. Same as in Figure 5 but for NGC 6553.

the map, with an abrupt transition occurring roughly along the line connecting the northeast and southwester corners of the map. The northwestern half of the map has $\Delta E(B-V)$ values as high as 0.15. Our map is remarkably similar to the appearance of the Cohen et al. (2014) HST-derived reddening map. The SW-NE division between high and low $\Delta E(B-V)$ possibly traces the southeastern edge of the dark cloud DCld 005.9–01.8 (Feitzinger & Stuewe 1984), while the high E(B-V) along the southern portion of the map appears to trace the northern edge of the TGU H77 P8 dark cloud (Dobashi 2006).

The reddening-corrected CMDs for NGC 6544 show significantly improved definition in the cluster sequences, with the g-i and u-r color dispersions being significantly decreased after applying the reddening corrections to the photometry. The proximity of the cluster allows us to trace stars that are at least two magnitudes fainter than the MSTO, although contamination from non-cluster stars along the MS is more likely because the disk MS and bulge RGB and MS both intersect the cluster CMD there, despite proper motion filtering.

5.6. NGC 6553 (Figure 10)

NGC 6553 is another extremely metal-rich GC that is regarded as the twin of NGC 6528 (Zoccali et al. 2001), with [Fe/H] = -0.18 from Harris (1996) and with more recent estimates as high as [Fe/H] = -0.10 (Montecinos et al. 2021). As with NGC 6528, NGC 6553 is projected toward Baade's Window. At a distance of $d_{\odot} = 5.2 \,\mathrm{kpc}$ (Montecinos et al. 2021), the cluster is within the Galactic bulge, 2.9 kpc from the Galactic center. As is the case with most of the clusters in this study, NGC 6553 suffers from field contamination, but like NGC 6528 it is located in Baade's window and has a relatively low E(B-V) zero-point. The differential reddening across the 20'. 6 \times 20'. 6 field is moderate at $\delta E(B-V) = 0.088$. Structurally, the map follows the same morphology as the one derived by Alonso-García et al. (2012), with two high extinction zones near the center of the map, immediately to the north and southeast of the cluster center. The largest deviations from $E(B-V)_0$ are in these two zones and in the far northern part of the map, with $\Delta E(B-V) \gtrsim 0.05$. The locations of excess $\Delta E(B-V) \approx 0.05$. -V) in the north and center of the map coincide with the projected position and extent of the dark cloud LDN 176. The southern part of the map shows slightly enhanced $\Delta E(B-V)$

and coincides spatially with the northern filament of dark cloud Dobashi 0236.

There is moderate enhancement in the definition of the cluster sequences when comparing CMDs before and after correcting the photometry for reddening. After correcting for reddening, the g, i diagram shows the signature of high [Fe/H] content—a curved RGB—, which can also be seen in the corrected g, i diagram of NGC 6528. The cluster is faint enough that the MSTO is intersected by the disk MS, which is prominent even after PM filtering, although the bulge RGB +MS are not evident in our CMDs.

5.7. NGC 6569 (Figure 11)

NGC 6569 is a compact bulge GC that is located in the Sagittarius region, only 3 kpc from the Galactic center. Harris (1996) gives a cluster metallicity of [Fe/H] = -0.76, which is consistent with newer estimates of -0.79 (Valenti et al. 2011) and -0.87 (Johnson et al. 2018). The average color excess toward this cluster is E(B-V) = 0.53 (Harris 1996) and Ortolani et al. (2001), or higher (E(B-V) > 0.55 mag; Johnson et al. 2018). The differential reddening map of the $16' \times 16'$ field around NGC 6569 shows that the color excess fluctuates on large scales, with coherent structures spanning over 10', as well as on scales down to several arcseconds. The pixel-topixel variation in color excess is significant at the $\delta E(B)$ -V) = 0.120 level. The most striking feature of the reddening map is a large structure that emanates from the southeast, nearly reaching the cluster center before bifurcating into two smaller north-south aligned filaments on either side of the cluster center. We find that the color excess inside this structure is at least 0.025 mag above the zero-point $E(B-V)_0$. NGC 6569 is projected toward the dark nebula LDN 305, and the highest column density of this cloud is southeast of the cluster center, consistent with the morphology of our reddening map.

Our cluster CMDs of NGC 6569 demonstrate tighter g-i and u-r color dispersions after correcting the photometry using the differential reddening map. The CMDs do not resolve the MSTO but extend from the RGB bottom to the TRGB, which in the g, i diagram is curved. This has been noted elsewhere (Ortolani et al. 2001) and is a feature of higher metallicity GCs. As was first noted in the V, I photometry of Ortolani et al. (2001) and also noticed in NIR/optical HST

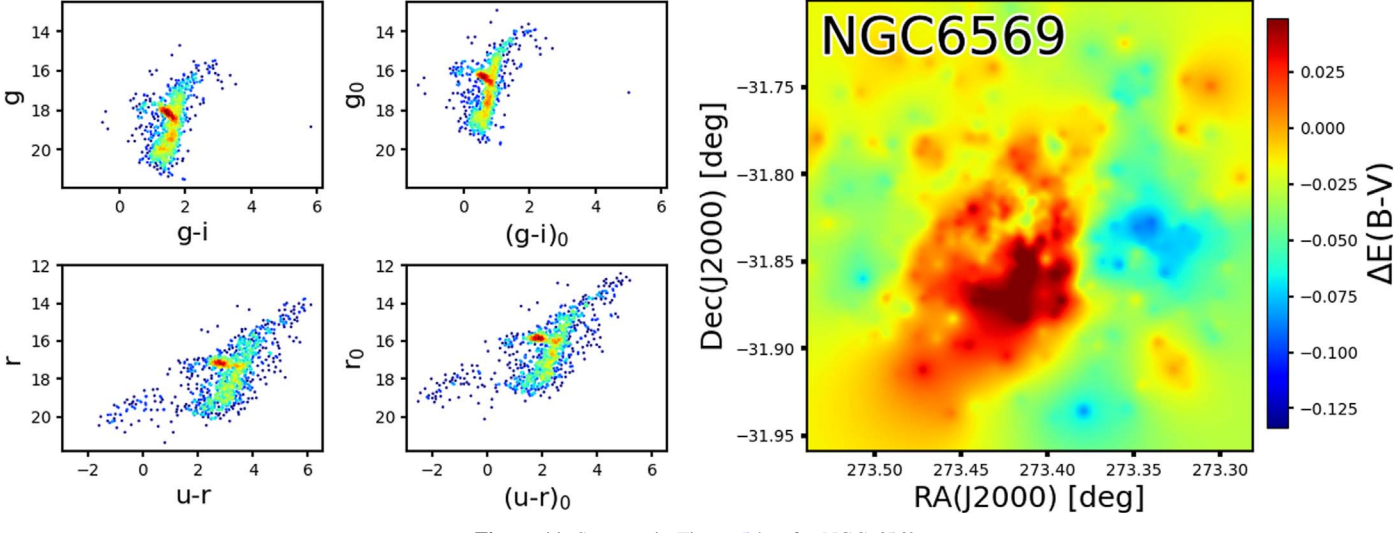


Figure 11. Same as in Figure 5 but for NGC 6569.

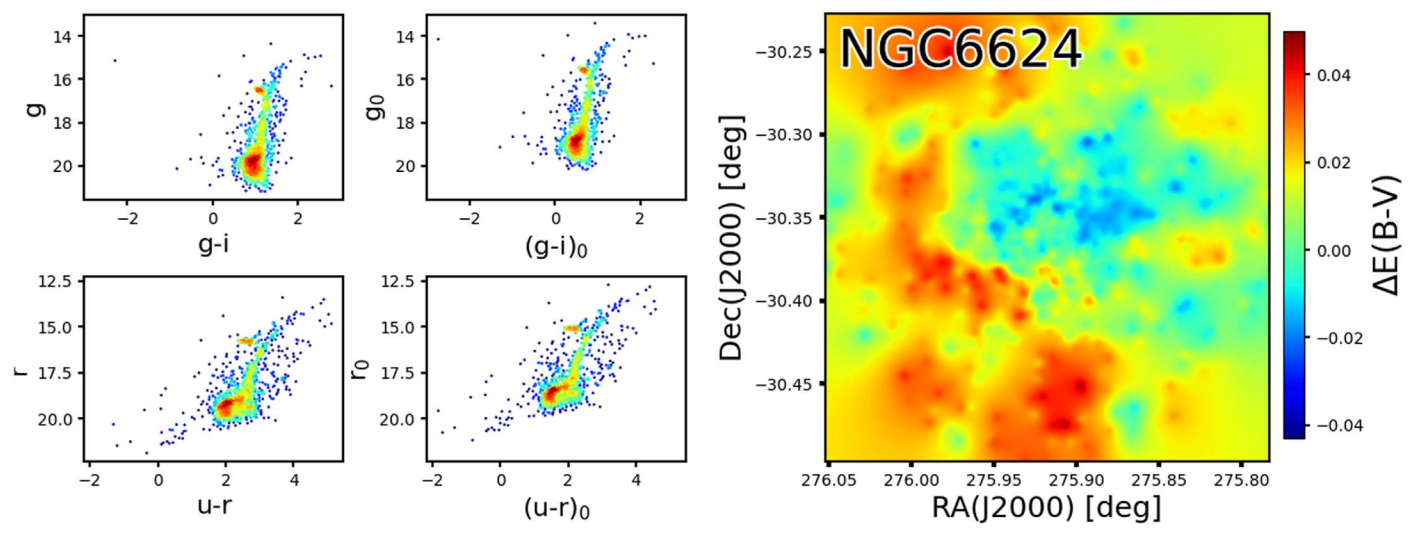


Figure 12. Same as in Figure 5 but for NGC 6624. Scaled between $-5\sigma_{E(B-V)}$ and $+3\sigma_{E(B-V)}$.

CMDs (Saracino et al. 2019), the cluster shows a dominant red HB at $g_0 = r_0 = 16$ mag. The red HB shows the canonical "tilt," which is common for high-metallicity clusters (Brocato et al. 1999). Our reddening-corrected CMDs confirm the presence of a prominent blue extension of the HB, as noticed in the HST photometry of Cohen et al. (2018) and later by Saracino et al. (2019), which is an unexpected feature for a metal-rich GC such as NGC 6569. Our photometry may be of insufficient precision to reproduce the double HB, which was investigated by Johnson et al. (2018). The u, r diagrams split the red HB from the red clump feature of the RGB.

5.8. NGC 6624 (Figure 12)

NGC 6624 is a compact core-collapsed GC at a distance of $d_{\odot}=7.9$ kpc in the outer Galactic bulge (Trager et al. 1995; Harris 1996; Saracino et al. 2016). Spectroscopic abundance estimates from Valenti et al. (2011) give [Fe/H]=-0.69, which is substantially lower than the -0.44 value from Harris (1996). However, in either case the cluster is relatively metalrich. NGC 6624 is perhaps most well known for being the

subject of many studies to identify and characterize exotic features in its dense core, such as X-ray bursts (Grindlay et al. 1976; King et al. 1993; Dalessandro et al. 2014) and radio pulsars (Biggs et al. 1994). There has even been recent debate concerning the presence of an intermediate mass black hole in the core of NGC 6624 (Perera et al. 2017; Baumgardt et al. 2019). The mean cluster color excess is given as E(B)-V) = 0.28 in Harris (1996), the same as derived via high resolution NIR photometry from Valenti et al. (2004) and the optical photometry from Richtler et al. (1994), which makes this one of the least obscured clusters in the sample. We find a correspondingly modest degree of differential reddening across the $16' \times 16'$ field centered on this cluster, with $\delta E(B)$ -V) = 0.070. The strongest reddening is in the northeast corner of the map, which reaches values 0.05 mag above the mean color excess. The south and southeastern portions also have elevated reddening at \sim 0.03-0.04 mag above the mean cluster reddening.

There is moderate improvement in the already very clean CMDs of NGC 6624, again, because the cluster does not suffer from significant differential reddening. The CMDs reach about

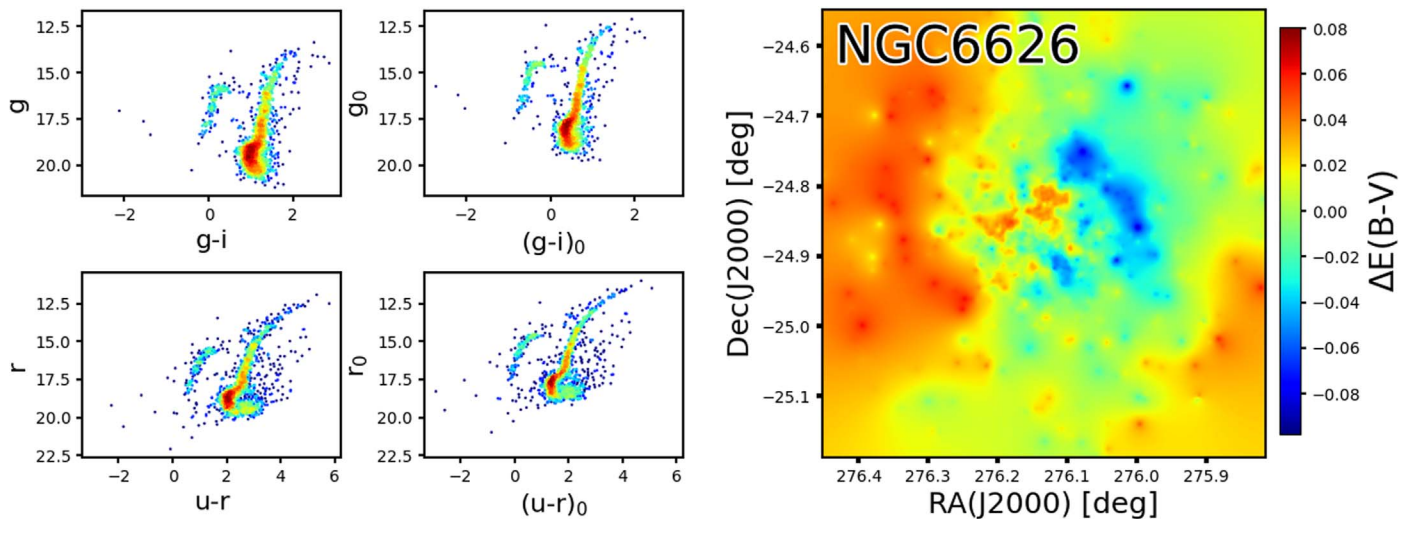


Figure 13. Same as in Figure 5 but for NGC 6626. Scaled between $-5\sigma_{E(B-V)}$ and $+3\sigma_{E(B-V)}$.

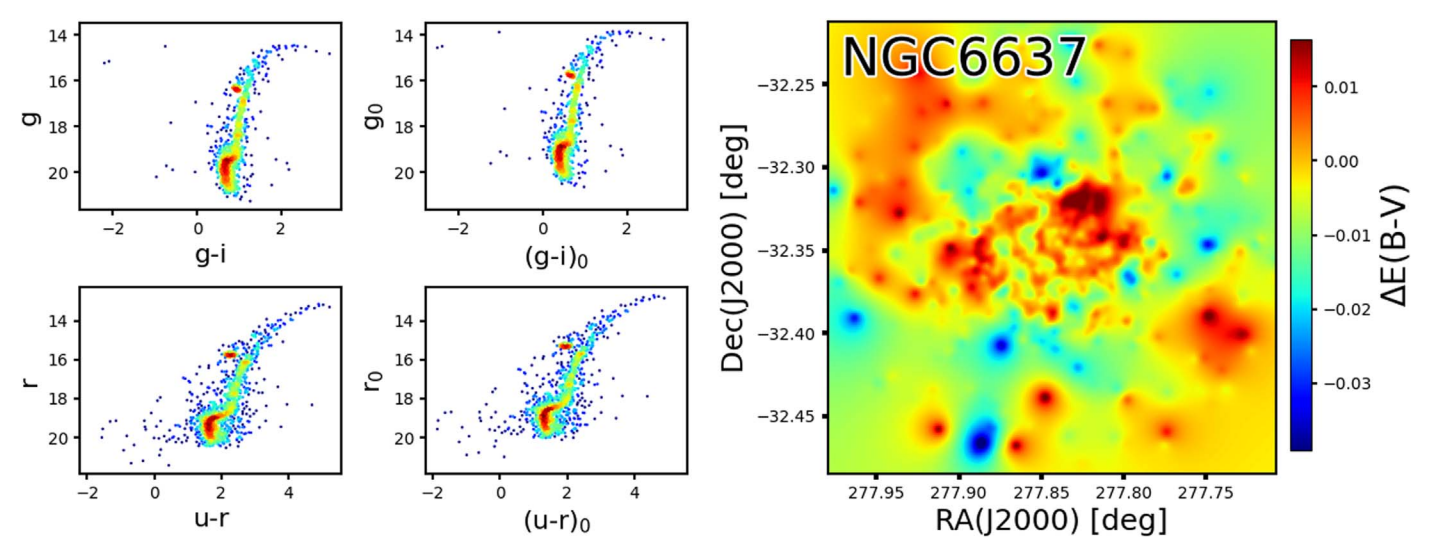


Figure 14. Same as in Figure 5 but for NGC 6637. Scaled between $-5\sigma_{E(B-V)}$ and $+3\sigma_{E(B-V)}$.

0.5 mag below the MSTO in g and r, and up to the TRGB. The corrected CMDs reveal the SGB, RGB, HB, and red clump.

5.9. NGC 6626 (Figure 13)

NGC 6626 (M28) is a massive, metal-poor bulge GC similar to NGC 6656 (M22) and NGC 6569. The metallicity of the cluster given by Harris (1996) is [Fe/H] = -1.32, which is nearly the same as the estimate of -1.33 derived from HST photometry by Kerber et al. (2018). Although the cluster is located 2.7 kpc from the Galactic center, its relatively high projected Galactic latitude ($b = -5^{\circ}.6$) means that sightlines do not suffer from substantial extinction. Harris (1996) gives E(B)-V) = 0.4, similar to E(B-V) = 0.38 derived from NIR photometry by Moni Bidin et al. (2021), but smaller than the value $E(B-V) \sim 0.44$ derived by Kerber et al. (2018). From our reddening map of the large $40' \times 40'$ field around NGC 6626, we find that the color excess fluctuates about the zero-point at the $\delta E(B-V) = 0.134$ level, similar to the range of E(B-V)values seen in the Moni Bidin et al. (2021) VVV map covering a slightly smaller area ($40' \times 30'$). Our reddening map reveals large-scale extinction in the eastern third of the field, which is

correlated with the north-westernmost edge of the dark cloud LDN 236. Parts of the cloud edge appear to break off into smaller filamentary structures that are aligned east—west, some of which reach toward the center of NGC 6626. The southern part of the map is above the average color excess, but not as high as the eastern portion.

The reddening-corrected photometry results in CMDs that show reduced color dispersion in all of the cluster sequences, most notably in the RGB and the well-populated blue HB. Our corrected CMDs reach about 1 mag below the MSTO, and up to the TRGB. There is residual contamination from bulge MS +RGB stars, redward of the cluster RGB and MS, even after PM filtering.

5.10. NGC 6637 (Figure 14)

NGC 6637 (M69) is another metal-rich bulge cluster, very similar in terms of CMD-derived age and metallicity to NGC 6624, both are only slightly more metal-rich than 47 Tuc (Heasley et al. 2000). The cluster is very near the Galactic center (1.7 kpc; Harris 1996), yet is projected at high Galactic latitude compared with most of our sample ($b = -10^{\circ}.3$), and

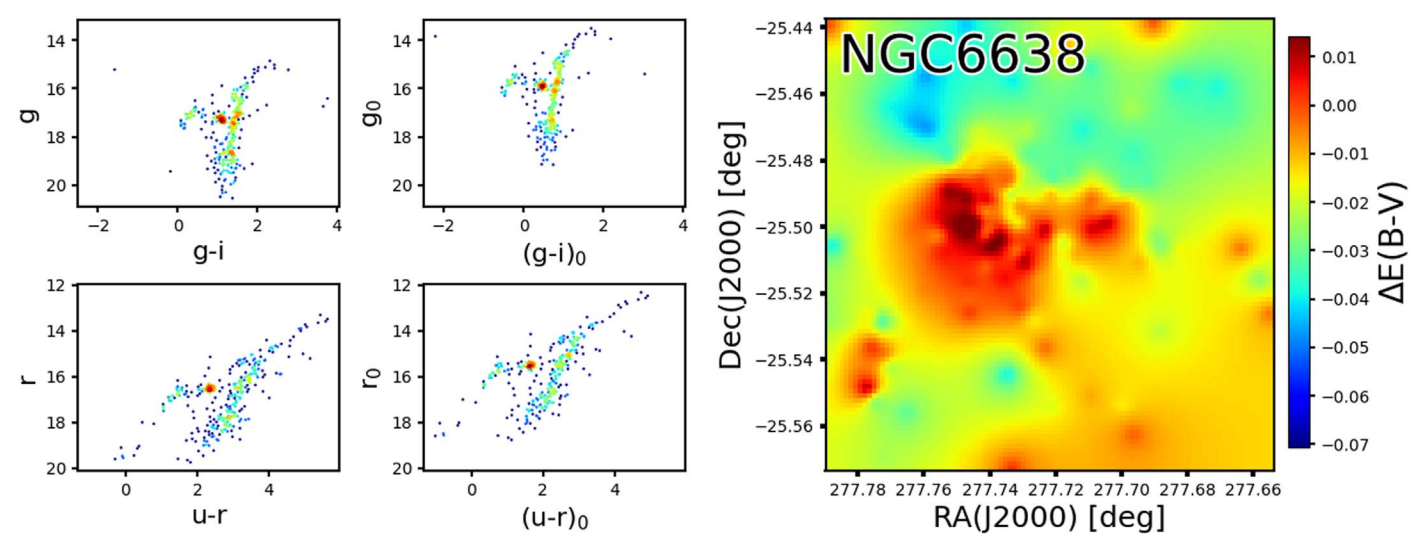


Figure 15. Same as in Figure 5 but for NGC 6638. Scaled between $-5\sigma_{E(B-V)}$ and $+3\sigma_{E(B-V)}$.

therefore has only a modest color excess zero-point of E(B-V)=0.18. We find from our $17'\times 17'$ map that the variations in color excess are correspondingly minimal, with $\delta E(B-V)=0.042$. The map shows high relative extinction (0.02 mag above the mean excess) at cluster-centric radii of r<4', similar to the map of Alonso-García et al. (2012). We also find higher than average extinction in the southwest and far north of the map.

The reddening-corrected CMDs of NGC 6637 are similar morphologically to those of NGC 6624, with a well-defined MSTO, SGB, RGB, and red HB, as well as a discernable red clump. For this cluster, we only reach about 0.5 mag below the MSTO, where field contamination is likely higher. Since the reddening toward this cluster is small and relatively uniform, we find that the position of the cluster stars is largely unchanged after correcting the photometry. However, the corrected CMDs do well in separating the AGB from the upper RGB.

5.11. NGC 6638 (Figure 15)

NGC 6638 is a metal-rich GC in the Galactic bulge, only 1.7 kpc from the Galactic center. Harris (1996) gives a metallicity of [Fe/H] = -0.95, similar to the NIR photometric estimate of [Fe/H] = -1.00 from Valenti et al. (2005). The zero-point color excess of this cluster is fairly significant and is given in Harris (1996) as E(B-V) = 0.41. From our $10' \times 10'$ reddening map, centered on NGC 6638, we find that the fluctuations in color excess are at the level of $\delta E(B-V) = 0.064$. The strongest reddening is near the center of the field, southeast of the cluster, and continues in that direction to the edge of the map. The maximum $\Delta E(B-V)$ is $\gtrsim 0.01$ mag. The structure of our map is consistent with the shape of the western edge of the dark nebula LDN 245.

There are clear improvements in the definition of the cluster sequences in the corrected CMDs. The cluster shows a clearly defined RGB, red clump, and an HB with a well-populated blue extension. The photometry reaches to the tip of the RGB but is not deep enough to identify the base of the RGB. The corrected CMDs have the morphological features that are expected of a high-metallicity cluster, such as a curved RGB and a red HB.

5.12. NGC 6642 (Figure 16)

NGC 6642 is a very old, highly concentrated, lowmetallicity bulge GC, located 1.7 kpc from the Galactic center. The Harris (1996) catalog gives a metallicity of [Fe/ H] = -1.26, while Minniti (1995) finds [Fe/H] = -1.40 from the spectra of 13 individual cluster stars. The BVI photometry of Barbuy et al. (2006) demonstrates that NGC 6642 is probably coeval with the halo GC M 5, meaning that NGC 6642 is one of the few metal-poor and old bulge GCs, and possibly one of the oldest fossils in the Galaxy. The mean color excess for this cluster is listed as E(B-V) = 0.4 in Harris (1996), which is a good match with the value of 0.42 derived by Barbuy et al. (2006). Our 14.6×14.6 reddening map centered on NGC 6642 was used to calculate the variations in color excess, which we find to be $\delta E(B-V) = 0.046$. The highest reddening ($\Delta E(B-V) \sim 0.02$) occurs along a curved filament originating in the northeast and terminating just north of the cluster center. This filament appears to be cospatial with the northern end of the arc-like dark nebula LDN 269, or possibly the westernmost end of the filamentary dark nebula LDN 284.

Significant improvement in the definition of the cluster stars is evident in the reddening-corrected CMDs. The CMDs are deep enough to trace the MSTO and cover the entire RGB extent up to the tip. There is a well-populated HB with a long blue extension, as well as a red clump. The corrected CMDs show a better defined RR-Lyrae gap between red and blue HB stars. It is apparent that field contamination is an issue at lower magnitudes, particularly redward of the SGB and MS, where the bulge evolutionary sequence intersects the cluster sequences.

5.13. NGC 6652 (Figure 17)

NGC 6652 is a very old, intermediate metallicity, compact GC located in the bulge at only 2.7 kpc from the Galactic center. The cluster has the highest projected Galactic latitude of our sample at $b=-11^{\circ}.38$. The optical CMD was first studied by Ortolani et al. (1994) and the cluster has since become famous for its exotic stellar content, which includes ultracompact X-ray binaries (Predehl et al. 1991; Deutsch et al. 2000;

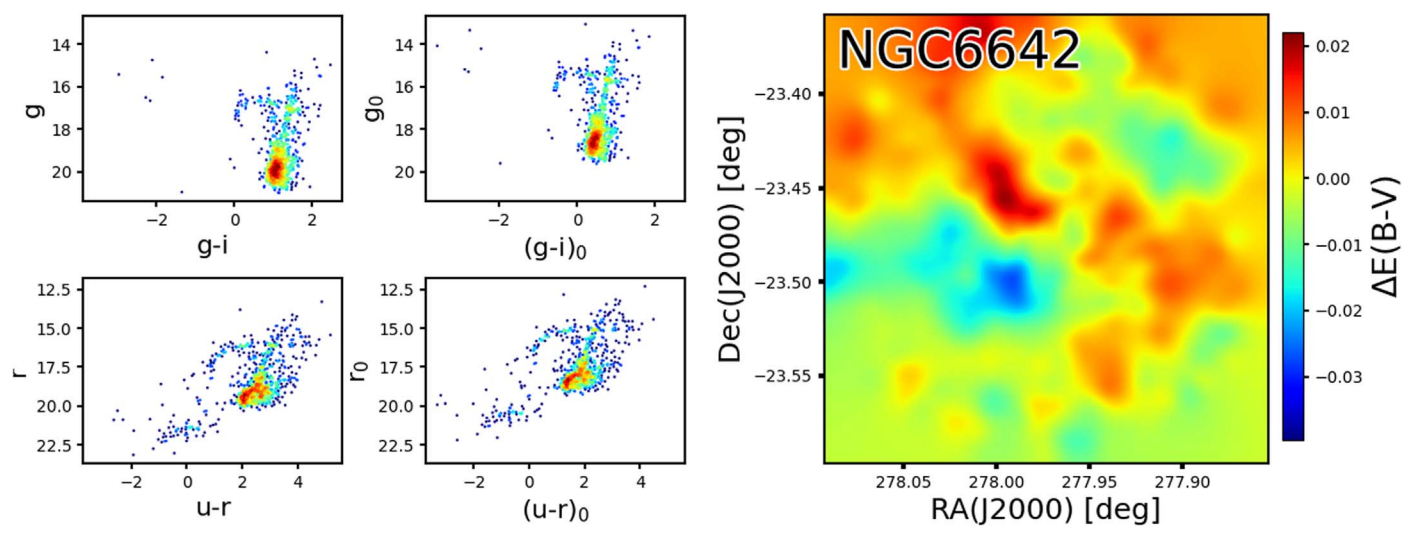


Figure 16. Same as in Figure 5 but for NGC 6642. Scaled between $-5\sigma_{E(B-V)}$ and $+3\sigma_{E(B-V)}$.

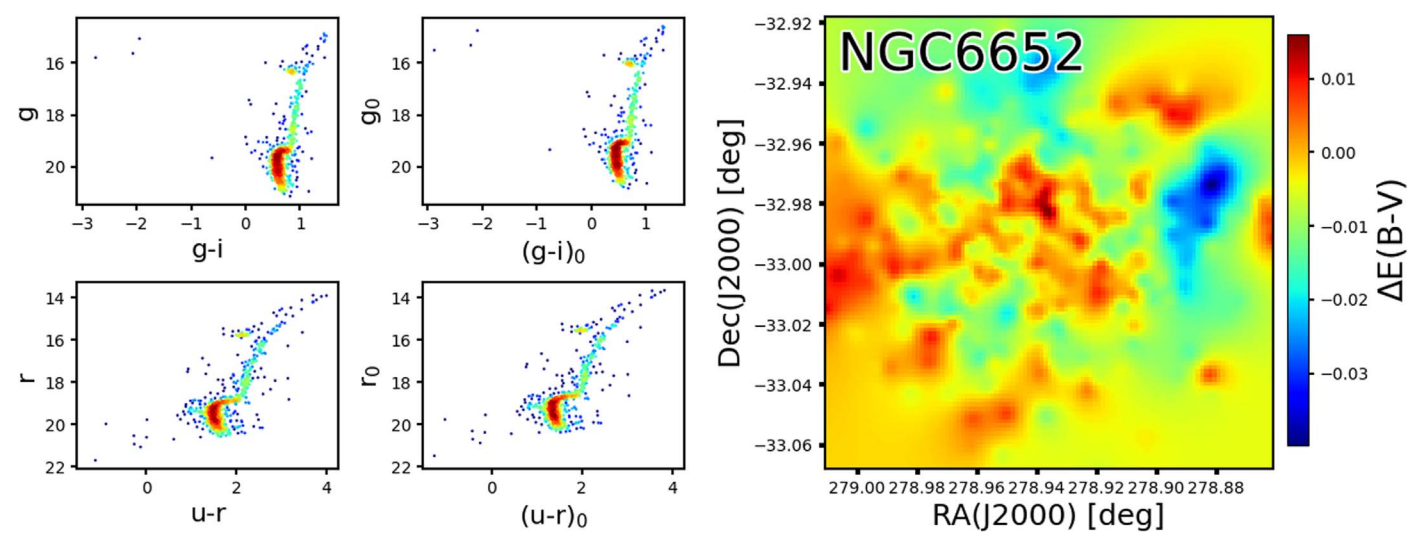


Figure 17. Same as in Figure 5 but for NGC 6652. Scaled between $-5\sigma_{E(B-V)}$ and $+3\sigma_{E(B-V)}$.

Stacey et al. 2012) and millisecond pulsars (DeCesar et al. 2015). Our 9.6 \times 9.6 map centered on NGC 6652 shows color excess variations on the level of $\delta E(B-V)=0.042$. Spatially, variations on the scale of \sim 0.6 dominate, with a general trend of higher extinction in the east and center of the map than elsewhere. The highest excess reddening, $\Delta E(B-V) \gtrsim 0.015$, is found in the center of the field. There are no known major Galactic dark nebulae extending to within the 10 r_h field of NGC 6652.

We find moderate improvement to the definition of the cluster CMDs after correcting for differential reddening, particularly in terms of the reduction in color dispersion of the MS in the g, i diagram. The photometry is of sufficient depth to go at least 1 mag below the MSTO, but we do not reach the MS knee. The SGB, MS, and HB are well populated, and some AGB stars are also visible. There are stars above the MSTO in the corrected CMDs, which are possibly part of the blue stragglers sequence, but we cannot rule out that these are contaminating disk MS stars.

5.14. NGC 6656 (Figure 18)

NGC 6656 (M22) is a fairly concentrated, massive, metalpoor Galactic GC that is projected toward the Galactic bulge but is probably a main disk or halo GC, which has a highly eccentric orbit and is near its perigalacticon (Dinescu et al. 1999; Chen et al. 2020). NGC 6656 is one of the nearest clusters to the Sun, at $d_{\odot} = 3.2 \,\mathrm{kpc}$ (Harris 1996), and has a large proper motion compared to the background bulge. This makes it a popular target for studies ranging from the search for a central IMBH (Kains et al. 2018) and nova remnants (Göttgens et al. 2019), to its variable star content (Alonso-García et al. 2021) and stellar dynamics (Chen et al. 2020). NGC 6656 is quite famous for its peculiar chemical content. Spectroscopic studies reveal a star-to-star spread in light element abundances (Marino et al. 2009; Lim et al. 2015). Spectroscopic studies have also revealed that NGC 6656 is one of a growing list of metal complex Galactic GCs (see Table 10 of Marino et al. 2015), with a spread in the [Fe/H] (Pilachowski et al. 1982) or bimodality in the [Fe/H]

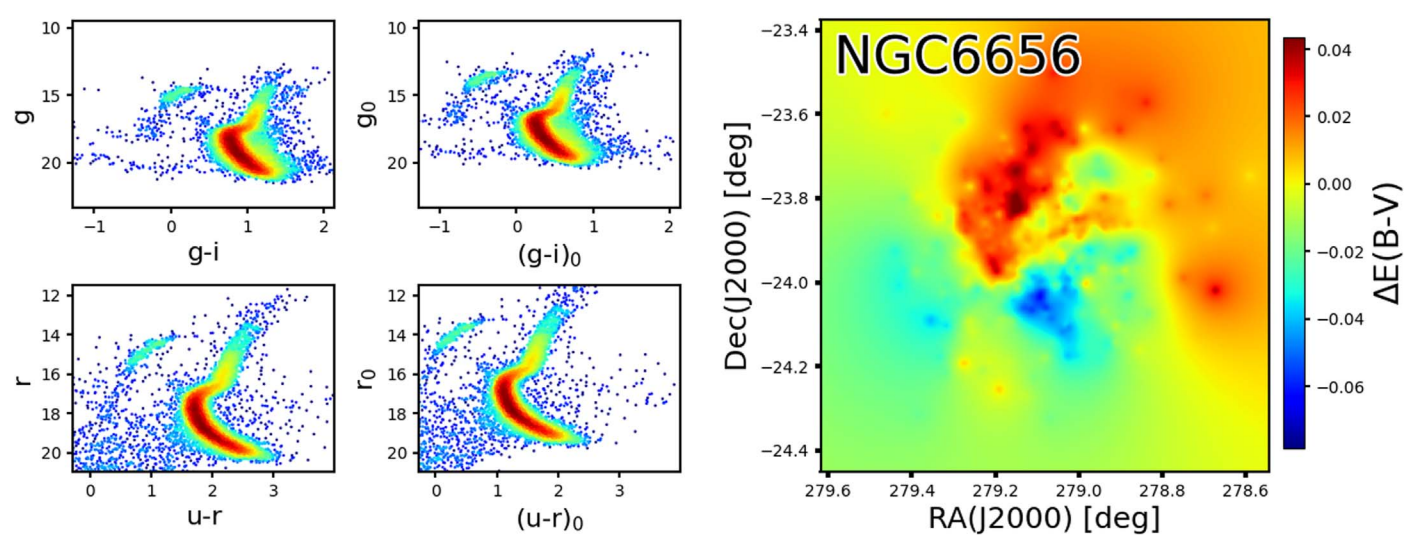


Figure 18. Same as in Figure 5 but for NGC 6656. Scaled between $-5\sigma_{E(B-V)}$ and $+3\sigma_{E(B-V)}$.

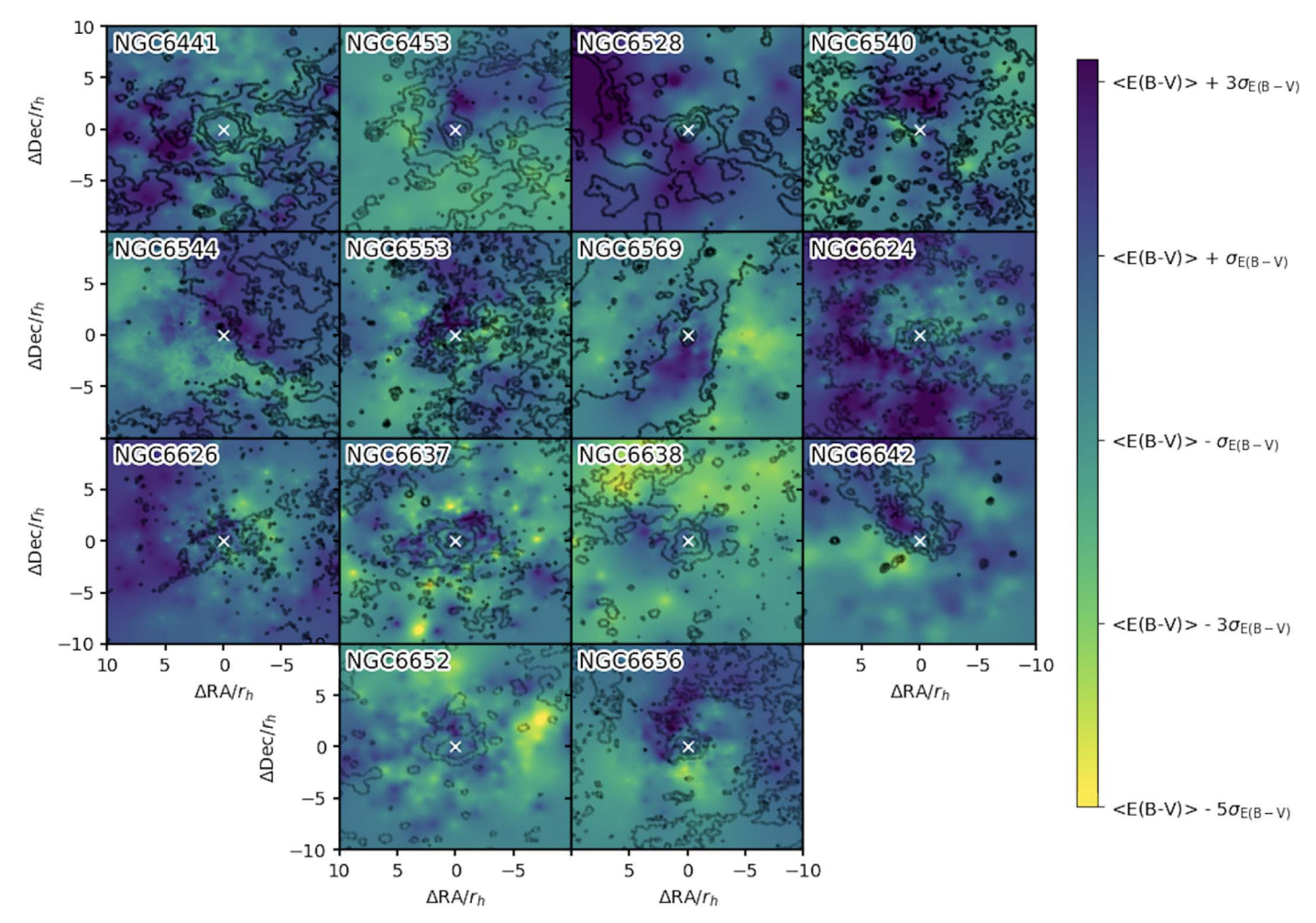


Figure 19. Extinction maps showing offset from zero-point color excess in units of $\sigma_{E(B-V)}$, which is the standard deviation in extinction values in each field. Black contours are WISE 12 μ m intensity levels which trace thermal continuum emission from warm dust. We find general agreement between our derived extinction maps and the maps of Galactic dust emission. North is up, east is to the left.

distribution (Marino et al. 2009, 2011). However, there has been some indication that differential reddening might affect studies of [Fe/H] variations (Ivans et al. 2004; Monaco et al. 2004). The average cluster metallicity is rather low, the

Harris (1996) value is [Fe/H] = -1.70. The reddening toward this cluster is E(B-V) = 0.34 from Harris (1996), which is close to the value 0.36 from Kunder et al. (2013). From our very large 1°.12 × 1°.12 reddening map, we find that

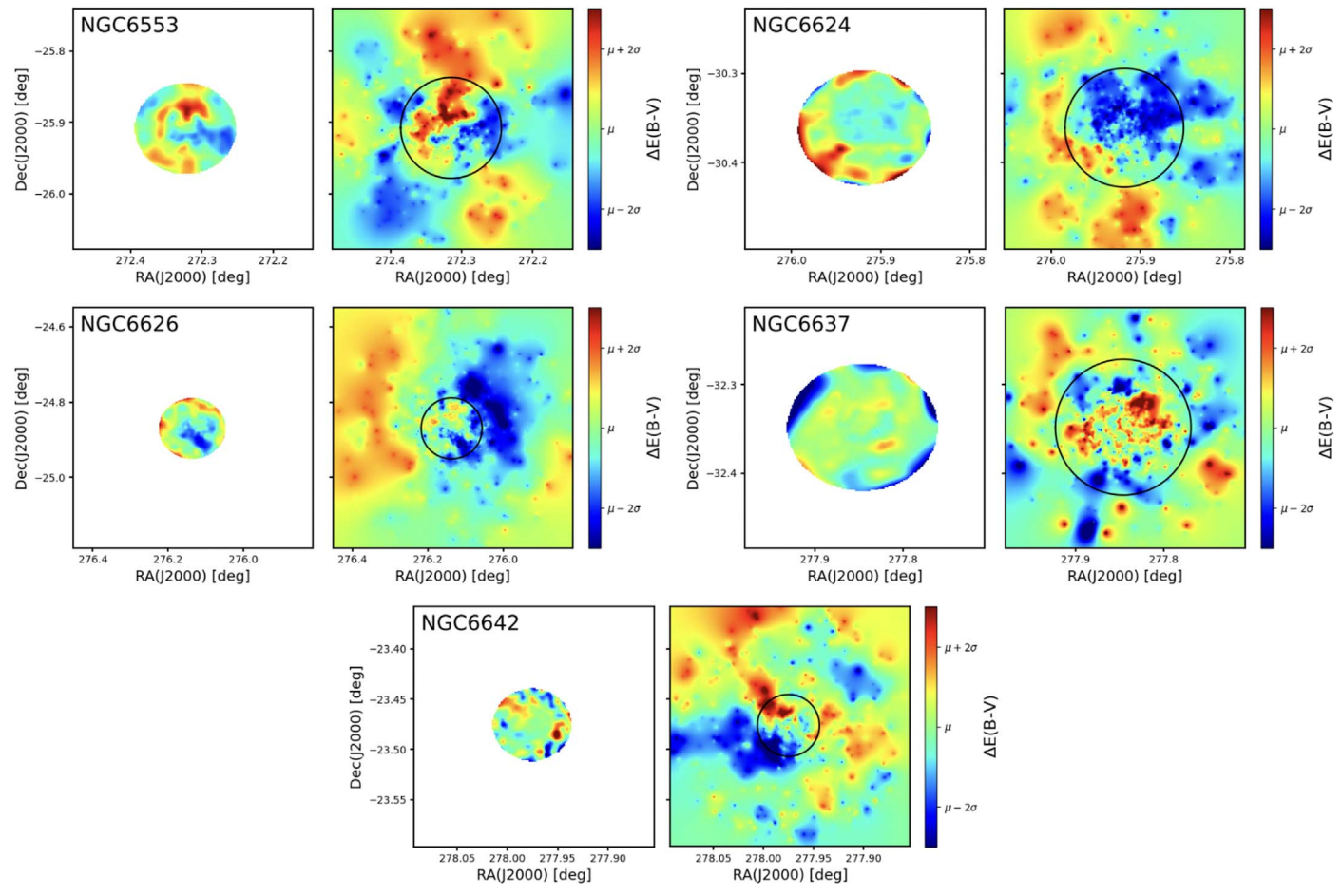


Figure 20. Side-by-side comparison between the reddening maps from Alonso-García et al. (2012; left-hand panels) and our own wide-field maps. The maps of differential color excess are scaled to $\pm 3\sigma$, with color bars shown to the right-hand of each cluster. The black circles overlaid on our maps indicate the spatial extent of the corresponding Alonso-García et al. (2012) maps. We find general agreement between our maps and those of Alonso-García et al. (2012) in terms of spatial structure. North is up, east is left.

the variations in color excess are moderate, with $\delta E(B-V) = 0.091$. Most striking in the map is a hook-like structure of high extinction that extends eastward from the western portion of the map until it curves southward into the central parts of the cluster. There is also rather large extinction in the southern portion of the map. The strongest color excess can be found along these structures ($\Delta E(B-V) \gtrsim 0.04$). The northern and southern features are cospatial with known dark clouds LDN 284 and LDN 263, respectively.

Owing to the proximity to this cluster, our CMDs trace the MS of the cluster almost two magnitudes below the MSTO, all the way to the TRGB. The blue HB of this cluster is very well populated. After applying reddening corrections to the photometry, we find a very clear signature of a split RGB in the r versus u-r CMD. The rectangular grid used to create the wide-field map for NGC 6656 has 15''-wide cells to save on computational cost.

6. Comparison with WISE MIR Images and Literature Maps

We verify our maps by comparing them with high resolution WISE 12 μ m continuum images (Wright et al. 2010) which trace thermal emission from warm diffuse Galactic dust. We construct isointensity contours from the WISE images, which are overlaid on our reddening maps in Figure 19.

In Figure 19, we show our color excess maps in units of $\sigma_{E(B-V)}$. Since the clusters span a very wide range in E(B-V)zero-points, a common absolute scale would result in some maps being washed out. The maps extend to cover a $20r_h \times 20r_h$ field around each cluster center, which is marked as a white cross. The black contours are isointensity levels from WISE 12, μ m images, which are sensitive to thermal continuum emission from warm diffuse Galactic dust. In several cases, we find remarkable spatial correlation between the dust contours and regions of enhanced color excess in our maps. The agreement that we find between enhanced reddening in our maps and dust emission is particularly striking in the cases of NGC 6453, NGC 6528, NGC 6544, NGC 6637, NGC 6642, and NGC 6656, where the dust emission is likely to be associated with known dark nebulae from Lynds (1962), which are specified in Section 5.

In the work of Alonso-García et al. (2012), the authors created differential reddening maps of 25 bright Galactic GCs toward the inner Galaxy using *B*, *V*, *I* broadband photometry from the Magellan 6.5 m Telescope and HST. We followed their technique to create maps by shifting cluster stars along the reddening vector in a CMD until they intersect a cluster fiducial ridge line, and then interpolate individual color excesses across the sky using bivariate regression. Six clusters were in common between their study and our own, namely, NGC 6553, NGC 6624, NGC 6626, NGC 6637, NGC 6642, and NGC 6656. In Figure 20, we present direct

comparisons between the maps from Alonso-García et al. (2012) and our own, for these six clusters, matched to the same spatial extent and scaled to their respective spans in $\Delta E(B-V)$.

The Alonso-García et al. (2012) maps have varying spatial scales, but in Figure 20 we simply interpolate their derived ΔE (B-V) values onto a regular rectangular grid. We find generally good agreement with the Alonso-García et al. (2012) maps in terms of both the spatial structure of the reddening and the estimated differential reddening scales.

7. Conclusions

We have used deep, wide-field photometry from the Blanco DECam Bulge Survey and Gaia EDR3 astrometry to derive color excess maps for 14 GCs toward the Galactic bulge, which reveal differential reddening on all scales ranging from 5" to tens of arcminutes caused by interstellar dust. Our maps efficiently correct for differential reddening for stars within 10 r_h of each cluster, resulting in higher definition CMDs. In the following list, we summarize the main results of this study of the differential reddening toward fourteen Galactic GCs toward the southern bulge:

- 1. The reddening maps accurately trace extinction by interstellar dust judging by their morphological similarity to the isocontours of WISE 12 μ m continuum images, which trace thermal emission from warm diffuse Galactic dust.
- The reddening maps are in good agreement with literature maps but have either a wider field of view or higher resolution than those found in the literature.
- 3. We find that after correcting for differential reddening, the cluster CMD sequences show less color dispersion and are better defined. In the cases of NGC 6637 and NGC 6656, splits in the RGB are already visible in the r versus u r diagrams without creating a Hess diagram or verticalizing the RGB.
- 4. After correcting for differential reddening, the cluster CMDs show broadening in excess of that expected from photometric measurement errors alone. This suggests that these clusters have star-to-star variations in atmospheric light element abundances.

Acknowledgments

The authors gratefully acknowledge financial support from the National Science Foundation under grants AST-1413755 and AST-1412673. A.J.K.H. gratefully acknowledges funding by the Deutsche Forschungsgemeinschaft (DFG, German Research Foundation)—Project-ID 138713538—SFB 881 ("The Milky Way System"), subprojects A03, A05, A11. A. M.K. acknowledges support from grant AST-2009836 from the National Science Foundation. C.I.J. gratefully acknowledges support from the HST Director's Discretionary Research Fund D0001.82494. Data used in this paper comes from the Blanco DECam Survey Collaboration. This project used data obtained with the Dark Energy Camera (DECam), which was constructed by the Dark Energy Survey (DES) collaboration. Funding for the DES Projects has been provided by the U.S. Department of Energy, the U.S. National Science Foundation, the Ministry of Science and Education of Spain, the Science

and Technology Facilities Council of the United Kingdom, the Higher Education Funding Council for England, the National Center for Supercomputing Applications at the University of Illinois at Urbana-Champaign, the Kavli Institute of Cosmological Physics at the University of Chicago, the Center for Cosmology and Astro-Particle Physics at the Ohio State University, the Mitchell Institute for Fundamental Physics and Astronomy at Texas A&M University, Financiadora de Estudos e Projetos, Fundaçõ Carlos Chagas Filho de Amparo á Pesquisa do Estado do Rio de Janeiro, Conselho Nacional de Desenvolvimento Científico e Tecnológico and the Ministério da Ciência, Tecnologia e Inovação, the Deutsche Forschungsgemeinschaft, and the Collaborating Institutions in the Dark Energy Survey. The Collaborating Institutions are Argonne National Laboratory, the University of California at Santa Cruz, the University of Cambridge, Centro de Investigaciones Enérgeticas, Medioambientales y Tecnológicas-Madrid, the University of Chicago, University College London, the DES-Brazil Consortium, the University of Edinburgh, the Eidgenössische Technische Hochschule (ETH) Zürich, Fermi National Accelerator Laboratory, the University of Illinois at Urbana-Champaign, the Institut de Cióncies de l'Espai (IEEC/CSIC), the Institut de Física d'Altes Energies, Lawrence Berkeley National Laboratory, the Ludwig-Maximilians Universität München and the associated Excellence Cluster Universe, the University of Michigan, the National Optical Astronomy Observatory, the University of Nottingham, the Ohio State University, the OzDES Membership Consortium the University of Pennsylvania, the University of Portsmouth, SLAC National Accelerator Laboratory, Stanford University, the University of Sussex, and Texas A&M University. Based on observations at Cerro Tololo Inter-American Observatory (2013A-0529; 2014A-0480; PI: Rich), National Optical Astronomy Observatory, which is operated by the Association of Universities for Research in Astronomy (AURA) under a cooperative agreement with the National Science Foundation. This work has made use of data from the European Space Agency (ESA) mission This publication makes use of data products from the Wide-field Infrared Survey Explorer, which is a joint project of the University of California, Los Angeles, and the Jet Propulsion Laboratory/California Institute of Technology, funded by the National Aeronautics and Space Administration. Gaia (https:// www.cosmos.esa.int/gaia), processed by the Gaia Data Processing and Analysis Consortium (DPAC,https://www.cosmos. esa.int/web/gaia/dpac/consortium.) Funding for the DPAC has been provided by national institutions, in particular the institutions participating in the Gaia Multilateral Agreement. This research has made use of the SIMBAD database, operated at CDS, Strasbourg, France, as well as the VizieR catalog access tool, CDS (DOI:10.26093/cds/vizier). The original description of the VizieR service was published in 2000, AAS 143, 23. This research has also made use of NASA's Astrophysics Data System Bibliographic Services. This work has made use of data from the European Space Agency (ESA) mission Gaia (https:// www.cosmos.esa.int/gaia), processed by the Gaia Data Processing and Analysis Consortium (DPAC, https://www.cosmos. esa.int/web/gaia/dpac/consortium). Funding for the DPAC has been provided by national institutions, in particular the institutions participating in the Gaia Multilateral Agreement.

Appendix Comparison with VVV Dust Maps

Here, we compare the VVV maps from Simion et al. (2017) to our own using common spatial and reddening scales. Eleven of the clusters in our program fall within the VVV survey footprint. Figures A1, A2, and A3 show side-by-side comparisons of the color excess maps from VVV (left) and this work (right) for NGC 6441, NGC 6453, NGC 6528, NGC

6540, NGC 6544, NGC 6553, NGC 6569, NGC 6624, NGC 6626, NGC 6638, and NGC 6642. The colorbar is scaled to $\pm 5\sigma$ from the mean E(B-V) computed from the VVV maps inside the white circle which has a radius of $10r_h$. In most cases, there is good agreement between the maps, but ours have $12\times$ the angular resolution (5" versus 1'). The clusters NGC 6637, NGC 6652, and NGC 6656 are partially or completely outside the VVV field and are not shown in the Appendix.

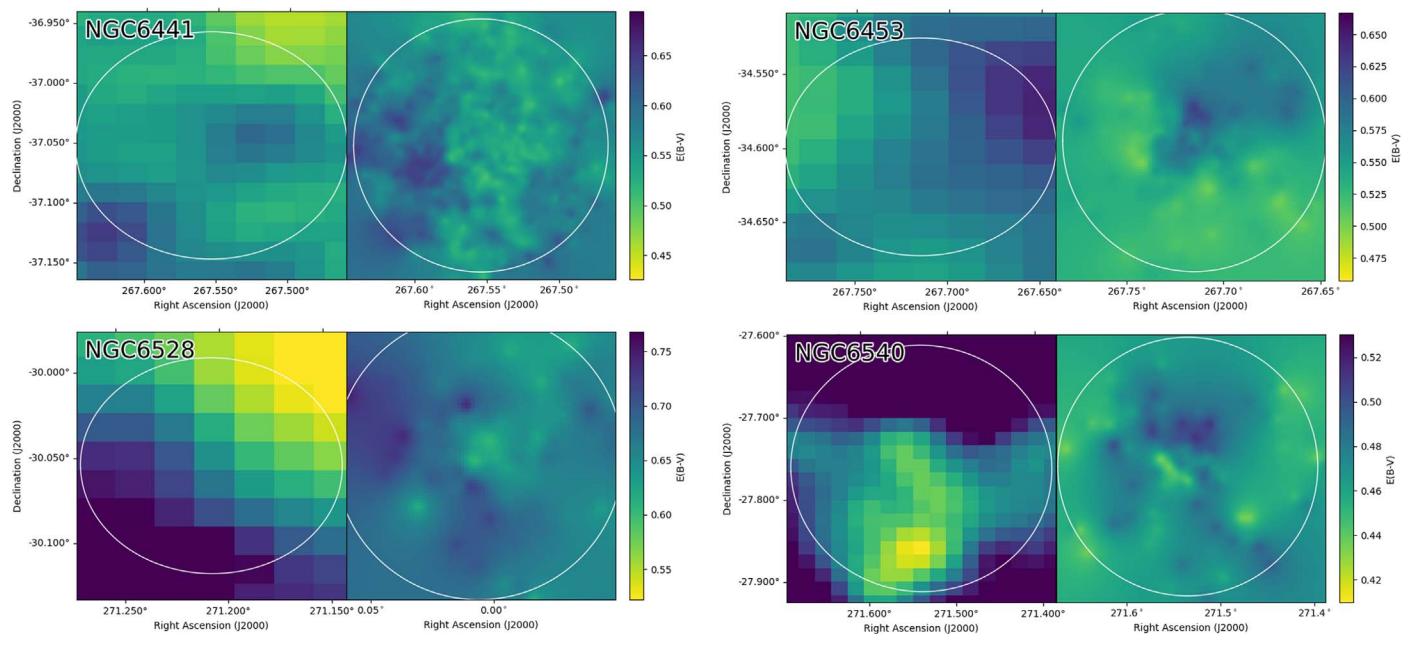


Figure A1. In this figure, we show comparisons for NGC 6441, NGC 6453, NGC 6528, and NGC 6540. The left-hand panels show the zoom-in of the VVV map, set to match the spatial scale of our reddening maps (right panels). The white circles have radius $10r_h$.

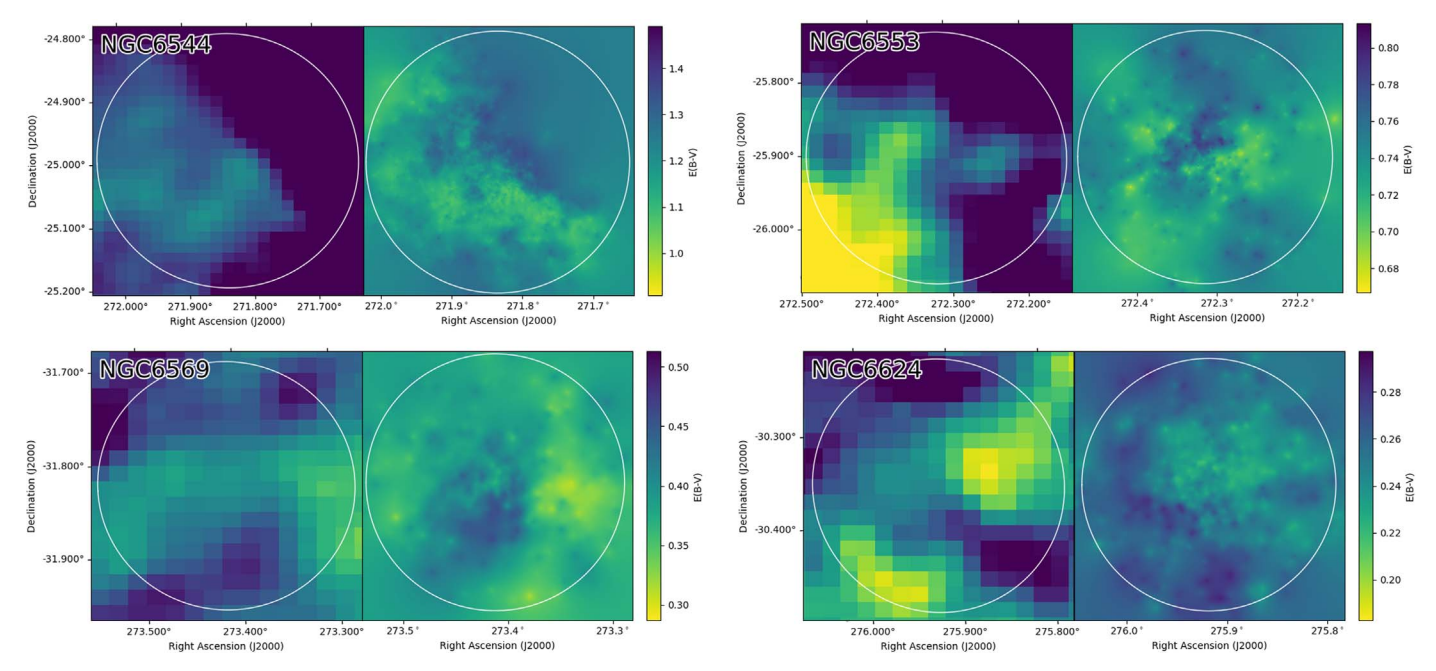


Figure A2. Same as Figure 21 but showing NGC 6544, NGC 6553, NGC 6569, and NGC 6624.

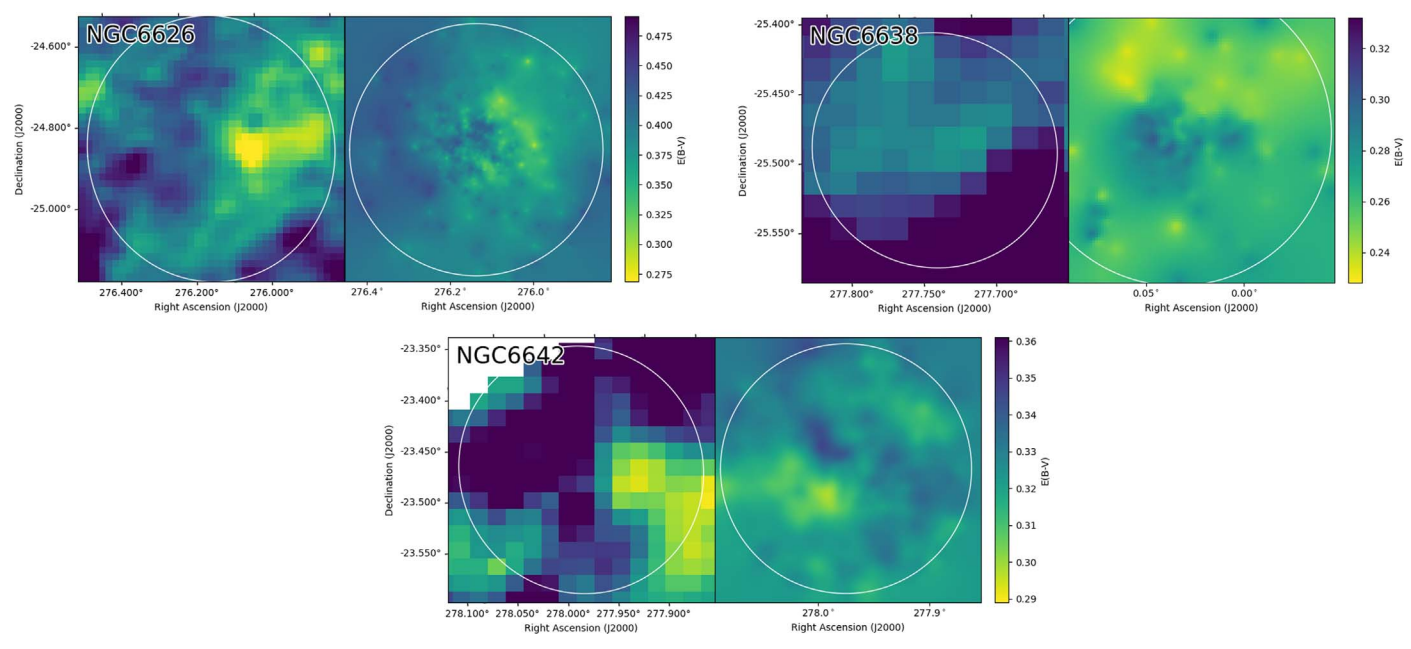


Figure A3. Same as Figure A1 but showing NGC 6626, NGC 6638, and NGC 6642.

ORCID iDs

Justin A. Kader https://orcid.org/0000-0002-6650-3757 Catherine A. Pilachowski https://orcid.org/0000-0002-3007-206X Christian I. Johnson https://orcid.org/0000-0002-8878-3315

R. Michael Rich https://orcid.org/0000-0002-8878-3515
R. Michael Rich https://orcid.org/0000-0003-0427-8387
Michael D. Young https://orcid.org/0000-0002-0036-941X
Iulia T. Simion https://orcid.org/0000-0001-8889-0762
William I. Clarkson https://orcid.org/0000-0002-2577-8885
Scott Michael https://orcid.org/0000-0002-2509-1197
Andrea Kunder https://orcid.org/0000-0002-2808-1370
Anna Katherina Vivas https://orcid.org/0000-0003-4341-6172

Andreas J. Koch-Hansen https://orcid.org/0000-0002-9859-4956

Tommaso Marchetti https://orcid.org/0000-0003-0064-0692

References

Alonso-García, J., Mateo, M., Sen, B., et al. 2011, AJ, 141, 146 Alonso-García, J., Mateo, M., Sen, B., et al. 2012, AJ, 143, 70 Alonso-García, J., Smith, L. C., Catelan, M., et al. 2021, A&A, 651, A47 Barbuy, B., Bica, E., Ortolani, S., et al. 2006, A&A, 449, 1019 Barnard, E. E., Frost, E. B., & Calvert, M. R. 1927, in A Photographic Atlas of Selected Regions of the Milky Way, ed. Gerald Orin Dobek (Washington, DC: Carnegie Institution of Washington) Baumgardt, H., He, C., Sweet, S. M., et al. 2019, MNRAS, 488, 5340 Bica, E., Ortolani, S., & Barbuy, B. 1994, A&A, 283, 67 Biggs, J. D., Bailes, M., Lyne, A. G., et al. 1994, MNRAS, 267, 125 Brocato, E., Castellani, V., Raimondo, G., et al. 1999, ApJ, 527, 230 Buitinck, L., Louppe, G., Blondel, M., et al. 2013, arXiv:1309.0238 Busso, G., Cassisi, S., Piotto, G., et al. 2007, A&A, 474, 105 Calamida, A., Bono, G., Lagioia, E. P., et al. 2014, A&A, 565, A8 Carretta, E., Cohen, J. G., Gratton, R. G., et al. 2001, AJ, 122, 1469 Chen, B.-Q., Huang, Y., Yuan, H.-B., et al. 2019, MNRAS, 483, 4277 Chen, D., Chen, L., & Wang, J. J. 2020, in IAU Symp. 351, Star Clusters: From the Milky Way to the Early Universe, ed. A. Bragaglia, M. Davies, A. Sills, & E. Vesperini (Cambridge: Cambridge Univ. Press), 422 Cohen, R. E., Mauro, F., Alonso-García, J., et al. 2018, AJ, 156, 41 Cohen, R. E., Mauro, F., Geisler, D., et al. 2014, AJ, 148, 18 Contreras Ramos, R., Zoccali, M., Rojas, F., et al. 2017, A&A, 608, A140

Dalessandro, E., Pallanca, C., Ferraro, F. R., et al. 2014, ApJL, 784, L29 DeCesar, M. E., Ransom, S. M., Kaplan, D. L., et al. 2015, ApJL, 807, L23 Deutsch, E. W., Margon, B., & Anderson, S. F. 2000, ApJL, 530, L21 Dinescu, D. I., Girard, T. M., & van Altena, W. F. 1999, AJ, 117, 1792 Dobashi, K. 2006, AstHe, 99, 620 Dutra, C. M., & Bica, E. 2002, A&A, 383, 631 Dutra, C. M., Santiago, B. X., Bica, E. L. D., et al. 2003, MNRAS, 338, 253 Feitzinger, J. V., & Stuewe, J. A. 1984, A&AS, 58, 365 Fitzpatrick, E. L. 1999, PASP, 111, 63 Gaia Collaboration, Brown, A. G. A., Vallenari, A., et al. 2021, A&A, 649, A1 Gaia Collaboration, Helmi, A., van Leeuwen, F., et al. 2018, A&A, 616, A12 Geisler, D., Villanova, S., O'Connell, J. E., et al. 2021, A&A, 652, A157 Gonzalez, O. A., Rejkuba, M., Zoccali, M., et al. 2011, A&A, 534, A3 Göttgens, F., Weilbacher, P. M., Roth, M. M., et al. 2019, A&A, 626, A69 Gran, F., Zoccali, M., Rojas-Arriagada, A., et al. 2021, MNRAS, 504, 3494 Gratton, R. G., Lucatello, S., Bragaglia, A., et al. 2007, A&A, 464, 953 Green, G. M., Schlafly, E. F., Finkbeiner, D., et al. 2018, MNRAS, 478, 651 Grindlay, J., Gursky, H., Schnopper, H., et al. 1976, ApJL, 205, L127 Harris, W. E. 1996, AJ, 112, 1487 Heasley, J. N., Janes, K. A., Zinn, R., et al. 2000, AJ, 120, 879 Ivans, I. I., Sneden, C., Wallerstein, G., et al. 2004, MmSAI, 75, 286 Johnson, C. I., Rich, R. M., Caldwell, N., et al. 2018, AJ, 155, 71 Johnson, C. I., Rich, R. M., Young, M. D., et al. 2020, MNRAS, 499, 2357 Kains, N., Calamida, A., Sahu, K. C., et al. 2018, ApJ, 867, 37 Kerber, L. O., Nardiello, D., Ortolani, S., et al. 2018, ApJ, 853, 15 King, I. R., Stanford, S. A., Albrecht, R., et al. 1993, ApJL, 413, L117 Kunder, A., Stetson, P. B., Cassisi, S., et al. 2013, AJ, 146, 119 Lim, D., Han, S.-I., Lee, Y.-W., et al. 2015, ApJS, 216, 19 Lynds, B. T. 1962, ApJS, 7, 1 Marchetti, T., Johnson, C. I., Joyce, M., et al. 2022, A&A, 664, A124 Marino, A. F., Milone, A. P., Karakas, A. I., et al. 2015, MNRAS, 450, 815 Marino, A. F., Milone, A. P., Piotto, G., et al. 2009, A&A, 505, 1099 Marino, A. F., Sneden, C., Kraft, R. P., et al. 2011, A&A, 532, A8 Massari, D., Koppelman, H. H., & Helmi, A. 2019, A&A, 630, L4 Melbourne, J., & Guhathakurta, P. 2004, AJ, 128, 271 Minniti, D. 1995, A&A, 303, 468 Minniti, D., Lucas, P. W., Emerson, J. P., et al. 2010, NewA, 15, 433 Monaco, L., Pancino, E., Ferraro, F. R., et al. 2004, MNRAS, 349, 1278 Moni Bidin, C., Mauro, F., Contreras Ramos, R., et al. 2021, A&A, 648, A18 Montecinos, C., Villanova, S., Muñoz, C., et al. 2021, MNRAS, 503, 4336 Ortolani, S., Bica, E., & Barbuy, B. 1994, A&A, 286, 444 Ortolani, S., Bica, E., & Barbuy, B. 1999, A&AS, 138, 267 Ortolani, S., Bica, E., & Barbuy, B. 2001, A&A, 374, 564 Perera, B. B. P., Stappers, B. W., Lyne, A. G., et al. 2017, MNRAS, 468, 2114 Pérez-Villegas, A., Barbuy, B., Kerber, L. O., et al. 2020, MNRAS, 491, 3251 Pilachowski, C., Leep, E. M., Wallerstein, G., et al. 1982, ApJ, 263, 187 Predehl, P., Hasinger, G., & Verbunt, F. 1991, A&A, 246, L21

Rich, R. M., Johnson, C. I., Young, M., et al. 2020, MNRAS, 499, 2340 Rich, R. M., Sosin, C., Djorgovski, S. G., et al. 1997, ApJL, 484, L25 Richtler, T., Grebel, E. K., & Seggewiss, W. 1994, A&A, 290, 412 Richtler, T., Grebel, E. K., Subramaniam, A., et al. 1998, A&AS, 127, 167 Saracino, S., Dalessandro, E., Ferraro, F. R., et al. 2016, ApJ, 832, 48 Saracino, S., Dalessandro, E., Ferraro, F. R., et al. 2019, ApJ, 874, 86 Schlafly, E. F., & Finkbeiner, D. P. 2011, ApJ, 737, 103 Schlegel, D. J., Finkbeiner, D. P., & Davis, M. 1998, ApJ, 500, 525 Schultheis, M., Ganesh, S., Simon, G., et al. 1999, A&A, 349, L69 Simion, I. T., Belokurov, V., Irwin, M., et al. 2017, MNRAS, 471, 4323 Stacey, W. S., Heinke, C. O., Cohn, H. N., et al. 2012, ApJ, 751, 62

```
Surot, F., Valenti, E., Hidalgo, S. L., et al. 2019, A&A, 629, A1
Trager, S. C., King, I. R., & Djorgovski, S. 1995, AJ, 109, 218
Valenti, E., Ferraro, F. R., & Origlia, L. 2004, MNRAS, 351, 1204
Valenti, E., Ferraro, F. R., & Origlia, L. 2010, MNRAS, 402, 1729
Valenti, E., Origlia, L., & Ferraro, F. R. 2005, MNRAS, 361, 272
Valenti, E., Origlia, L., & Rich, R. M. 2011, MNRAS, 414, 2690
Vasiliev, E. 2019, MNRAS, 484, 2832
von Braun, K., & Mateo, M. 2001, AJ, 121, 1522
Vulic, N., Barmby, P., & Gallagher, S. C. 2018, MNRAS, 473, 4900
Wright, E. L., Eisenhardt, P. R. M., Mainzer, A. K., et al. 2010, AJ, 140, 1868
Zoccali, M., Renzini, A., Ortolani, S., et al. 2001, AJ, 121, 2638
```